# Revealing Ultrafast Population Transfer Between Nearly Degenerated Electronic States

Pascal Heim,[†,§] Sebastian Mai,[‡,¶,§] Bernhard Thaler,[†] Stefan Cesnik,[†] Davide Avagliano,[‡] Dimitra Bella-Velidou,[‡] Wolfgang E. Ernst,[†] Leticia González,[*,‡] and Markus Koch[*,†]

[†]*Graz University of Technology, Institute of Experimental Physics, Petersgasse 16, A-8010 Graz, Austria*

[‡]*University of Vienna, Faculty of Vienna, Institute of Theoretical Chemistry, Währinger Str. 17, A-1090 Vienna, Austria*

[¶]*Present Address: Vienna University of Technology, Photonics Institute, Gußhausstr. 27–29, A-1040 Vienna, Austria*

[§]*These authors contributed equally to this work*

E-mail: leticia.gonzalez@univie.ac.at; markus.koch@tugraz.at

**Abstract**

The response of a molecule to photoexcitation is governed by the coupling of its electronic states. However, if the energetic spacing between the electronically excited states at the Franck–Condon window becomes sufficiently small, it is infeasible to selectively excite and monitor individual states with conventional time-resolved spectroscopy, preventing insight into the energy transfer and relaxation dynamics of the molecule. Here, we demonstrate how the combination of time-resolved spectroscopy and extensive surface hopping dynamics simulations with a global fit approach on individually-excited ensembles overcomes this limitation and resolves the dynamics in the n3p Rydberg states in acetone. Photoelectron transients of the three closely spaced states $n3p_x$, $n3p_y$, and $n3p_z$ are used to validate the theoretical results, which in turn allow retrieving a comprehensive kinetic model describing the mutual interactions of these states for the first time.

# Graphical TOC Entry
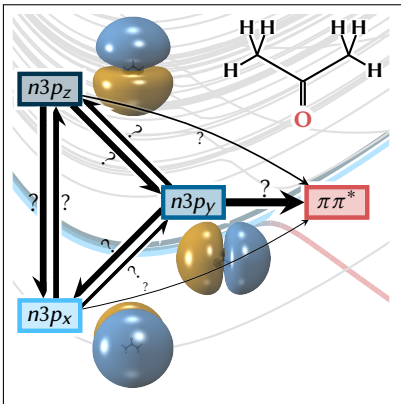
The mechanistic understanding of the initial processes in light-induced molecular excited-state dynamics is both of fundamental interest and essential for the development of various technological applications, for example efficient light harvesting systems[1] or molecular machines.[2] The first steps of these dynamics, which proceed in the femto- to picosecond range, are often accompanied by nonadiabatic population transfer between the excited states and can therefore be observed in real time with ultrafast time-resolved spectroscopy.[3] Such spectroscopy, in conjunction with state-of-the-art excited-state computational chemistry methods has revealed general concepts for understanding excited-state interactions in molecules[4–7] by using static[8,9] as well as dynamic[10,11] approaches. Nevertheless, following the nonadiabatic dynamics of molecules becomes rather challenging when the energy differences between excited electronic states within the Frack–Condon window becomes small. Although in polyatomic molecules the density of states is generally large, the situation can be particularly demanding in transition metal complexes,[12,13] extended biomolecules,[14] or within the Rydberg manifolds of small molecules, where not only higher-lying states in the Rydberg series are close in energy,[15] but also occasionally low-lying states,[16] especially if they have the same principal quantum number (e.g., $n3p_x$, $n3p_y$, $n3p_z$). Spectroscopic observation of the dynamical behaviour of the individual states is then often buried under the "averaged" population decay of all states within the particular energetic region. These experimental difficulties have two reasons. First, the energetic proximity of the states in combination with the spectral width of sufficiently short laser pulses does not allow exciting single electronic states, but rather creates a complex distribution of population in multiple states. Second, simple sequential or parallel decay models, which can be routinely applied in data analysis via global fitting routines in simpler situations,[17–20] cannot accommodate complex relaxation pathways and state mixing due to multiple couplings. These two issues obscure the nonadiabatic processes occurring within a dense set of states, requiring specialized approaches to obtain a comprehensive mechanistic understanding of the energy transfer in certain molecules.

In this work, we demonstrate that the combination of time-resolved photoelectron spec-
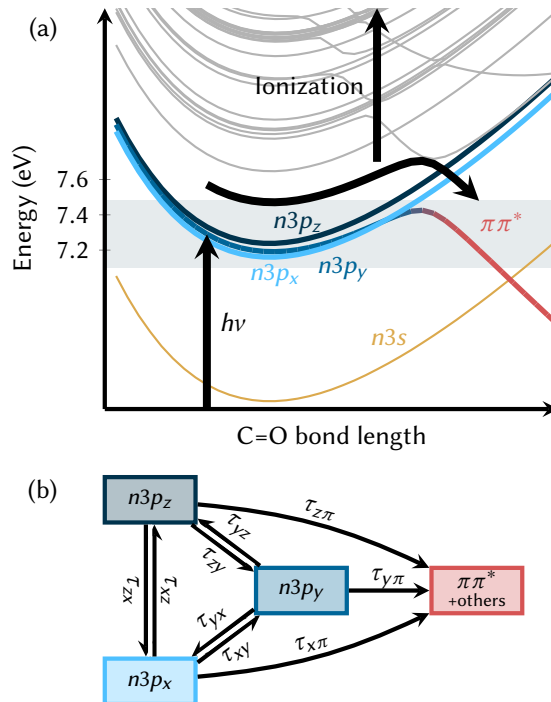
Figure 1: (a) Schematic overview of the relevant potential energy surfaces of acetone excited states, including the n3p and $\pi\pi^*$ states. (b) Basic kinetic model assumed for the nonadiabatic dynamics among the acetone n3p and $\pi\pi^*$ states with the nine considered time constants.

troscopy (TRPES)[21,22] and surface hopping simulations with the SHARC method[11] is able to fully characterize the dynamics in the regime of multiple nearly degenerate electronic states. Specifically, we are resolving the population transfer dynamics in the n3p Rydberg manifold of the acetone molecule after two-photon excitation. The photophysical and photochemical processes involving acetone have been in the limelight since the early days of femtochemistry,[23–25] with a recent renaissance[15,26–30] motivated by the importance of acetone as the simplest aliphatic ketone. The difficulty of resolving light-induced processes in acetone derives from its electronic structure, characterized by series of Rydberg states that are strongly coupled to valence states, with the consequence of complex nonadiabatic relaxation dynamics where the electronic population is cascading down the ladder of Rydberg states.[15,28,30–32] As shown schematically in Fig. 1a, the n3p manifold, energetically located at the lower end of the Rydberg series, consists of the three states n3p$_x$ ($A_2$, 7.34 eV), n3p$_y$ ($A_1$, 7.40 eV), and n3p$_z$ ($B_2$, 7.45 eV),[16] lying within about 100 meV in the Franck-Condon region of the ground

4

state. This manifold of states was investigated in time-resolved experiments and is considered to play an important role in the population transfer to lower states.[26,27,29] The energetic proximity of the three n3p states leads to significant vibrational coupling and—together with the presence of symmetry-dependent couplings with the $\pi\pi^*$ ($A_1$) valence state—a complex interaction among all these states.[33–37] As a consequence, the dynamics of the individual n3p states within this dense region has evaded detailed observation so far, despite the importance of the n3p manifold as the bottleneck for the radiationless deactivation pathways of the higher-lying Rydberg states.

Here, we solve this problem and follow the transient population of the acetone n3p Rydberg states after excitation in terms of the individual nonadiabatic transition time scales between the four most important states: n3p$_x$, n3p$_y$, n3p$_z$, and $\pi\pi^*$. We note here that it was previously shown in the literature[29,32] that also other dark states (n$\pi^*$, n3s) might be involved in the dynamics. Hence, in the kinetic model fits, our label "$\pi\pi^*$" collectively includes also those dark states, although the $\pi\pi^*$, n$\pi^*$, and n3s states are explicitly present in both the experiments and the simulations. The transition time scales between the four states are summarized in Fig. 1b, which shows the six inter-Rydberg time constants ($\tau_{xy}$, $\tau_{yx}$, $\tau_{xz}$, $\tau_{zx}$, $\tau_{yz}$, $\tau_{zy}$) and the three Rydberg decay time constants ($\tau_{x\pi}$, $\tau_{y\pi}$, $\tau_{z\pi}$) considered here. We describe the population dynamics by the following system of differential equations representing a unimolecular first-order kinetic model:

$$\frac{\partial}{\partial t}\vec{P} = \mathbf{M}\vec{P} + g(t)\vec{P}_0,\tag{1}$$

where $\vec{P} = (P_{n3p_x}(t), P_{n3p_y}(t), P_{n3p_z}(t), P_{\pi\pi^*}(t))^T$ is the vector containing the time-dependent

state populations. The coupling matrix $\mathbf{M}$ contains the nine time constants:

$$\mathbf{M} = \begin{pmatrix} -\frac{1}{\tau_{xy}} - \frac{1}{\tau_{xz}} - \frac{1}{\tau_{x\pi}} & +\frac{1}{\tau_{yx}} & +\frac{1}{\tau_{zx}} & 0 \\ +\frac{1}{\tau_{xy}} & -\frac{1}{\tau_{yx}} - \frac{1}{\tau_{yz}} - \frac{1}{\tau_{y\pi}} & +\frac{1}{\tau_{zy}} & 0 \\ +\frac{1}{\tau_{xz}} & +\frac{1}{\tau_{yz}} & -\frac{1}{\tau_{zx}} - \frac{1}{\tau_{zy}} - \frac{1}{\tau_{z\pi}} & 0 \\ +\frac{1}{\tau_{x\pi}} & +\frac{1}{\tau_{y\pi}} & +\frac{1}{\tau_{z\pi}} & 0 \end{pmatrix}, \tag{2}$$

and $g(t)\vec{P}_0$ is the source term that populates the states (containing the temporal profile of the laser excitation $g(t)$ and a state-dependent prefactor $\vec{P}_0$). The main goal of our study is to assign the numeric values of the nine time constants and to investigate their dependence on the excitation energy. This task can only be achieved by a combination of experiment and simulation. The experiment can only observe "effective" time constants $\tau_m$, which are related to the eigenvalues $\lambda_m$ of the coupling matrix $\mathbf{M}$ by $\tau_m = \lambda_m^{-1}$ (in the following, $m$ enumerates the eigenvalues of $\mathbf{M}$). These effective time constants correspond to the so-called decay associated spectra (DAS),[17–20] discussed in detail in section S1 in the supporting information (SI). As we do not consider the decay of the $\pi\pi^*$ state here, one eigenvalue of $\mathbf{M}$ is always zero (i.e., one effective time constant is infinite), leaving in principle three time constants that could be obtained from the experiment. In contrast, appropriate nonadiabatic dynamics simulations can directly access the electronic populations of each individual state, what allows obtaining all nine individual time constants from a suitable global fit. The effective time constants derived from the simulated coupling matrix can then be compared to the experimental ones to verify the accuracy of the simulations.

In the TRPES experiments, isolated acetone molecules are excited into the n3p manifold by two-photon pump excitation (320 to 336 nm) and the transient population is probed after a variable time delay via one-photon probe photoionization (402 nm). The time-resolved photoelectron spectrum (see section S2 in the SI for details on the energy calibration) for 333 nm excitation is exemplarily shown in Fig. 2 (see section S3 in the SI for results at other excitation wavelengths). In the spectrum, the n3p$_x$, n3p$_y$ and n3p$_z$ states are observed as
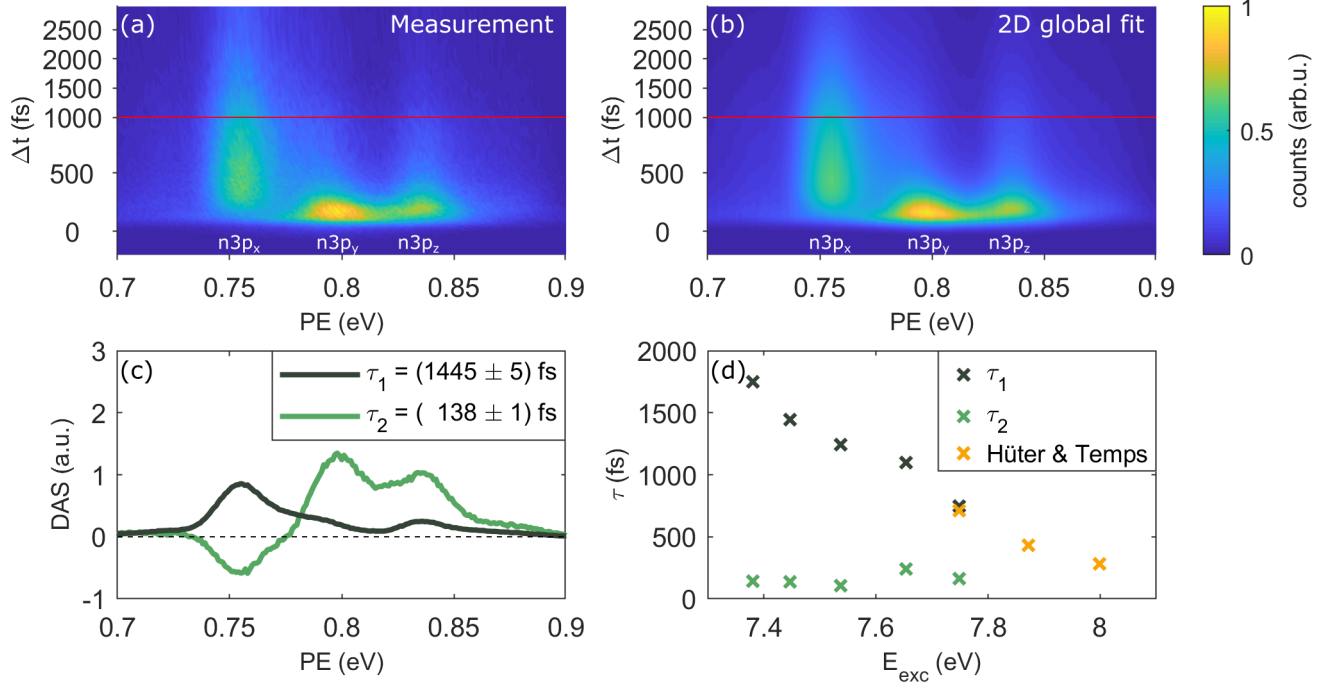
6

Figure 2: Overview of the experimental results. Measured transient photoelectron spectra (a), the 2D global fit of the spectrum (b) with corresponding DAS (c) for 333 nm pump wavelength ($E_{\text{exc}} = 7.44\,\text{eV}$). Panel (d) shows the time constant dependence over excitation energy, including three data points from Hüter and Temps.[27] The red lines in (a) and (b) indicate a change of the vertical axis scale. PE: photoelectron kinetic energy; E: Two-photon excitation energy.

separated photoelectron bands. The photoelectron kinetic energies (probe photon energy plus state energy minus ionization potential, see section S2 in the SI) of the three bands are centered at approximately 0.75, 0.80, and 0.84 eV, respectively. The narrow Franck-Condon envelope of the three bands indicates Rydberg state ionization to the ionic ground state with a $\Delta\nu = 0$ propensity rule. The n3p$_y$ and n3p$_z$ states are simultaneously populated at $t = 0$ fs and show similar signal increase and decrease. In contrast, the n3p$_x$ signal behaves differently, building up later and decreasing much slower.

We fit the measured photoelectron spectrum $S(E, t)$ (Fig. 2a) with a 2D global fit routine to the following function:[17–20]

$$S(E,t) = \sum_m g(t) \circledast \left( \Theta(t) \text{e}^{-\frac{t}{\tau_m}} \right) \text{DAS}_m(E) \tag{3}$$

7

where $\Theta(t)$ is the Heaviside step function, $\tau_m = \lambda_m^{-1}$ are the effective time constants, and $\text{DAS}_m(E)$ are the decay-associated spectra (see section S1 in the SI). By varying the number of decay-associated spectra and time constants contained in the global fit, we find that $m = \{1, 2\}$ (fit shown in Fig. 2b) is sufficient and $m = \{1, 2, 3\}$ does not increase the fit quality. This finding reflects the apparent similarity of the n3p$_y$ and n3p$_z$ transient signals. Hence, it appears that two of the three relevant effective time constants are very similar, and that two time constants are sufficient to describe the time-resolved photoelectron spectrum. The two corresponding DAS (Fig. 2c) confirm that n3p$_y$ and n3p$_z$ behave very similar, as given by the two peaks of the DAS corresponding to $\tau_2$. Consequently, we can assign the larger constant $\tau_1$ to the decay of n3p$_x$, and the smaller constant $\tau_2$ to the parallel decay of the n3p$_y$ and n3p$_z$ states. Unfortunately, the DAS does not allow uncovering more details of the complex population transfer between the different n3p states other than a population transfer from n3p$_y$ and n3p$_z$ to n3p$_x$ which is indicated by a negative DAS amplitude of the fast time constant.

The dependence of the effective time constants on the excitation energy is plotted in Fig. 2d. Whereas $\tau_2$ seems to remain constant at about 150 fs, $\tau_1$ is strongly energy-dependent and decreases from about 1800 fs to 700 fs upon increasing the pump energy. At the highest excitation energy (7.75 eV), our values of $\tau_1$ show very good agreement with the results of Hüter and Temps.[27] Moreover, time constants reported by these authors for higher energies show a consistent behaviour in the energy dependence. Unfortunately, their energy resolution did not allow separating the different n3p states, so that they did not report decay constants that could be compared to our $\tau_2$ values.

As the experiment cannot obtain the individual matrix elements of $\mathbf{M}$, we performed nonadiabatic dynamics simulations using the surface hopping approach SHARC.[11,38] The potential energy surfaces were described employing a linear vibronic coupling (LVC) model[39] composed of 49 diabatic electronic states, including all states from the $S_0$ ground state to the $\pi\pi^*$ state, which is the S$_{48}$ at the Franck-Condon geometry. We propagated (see Section S4
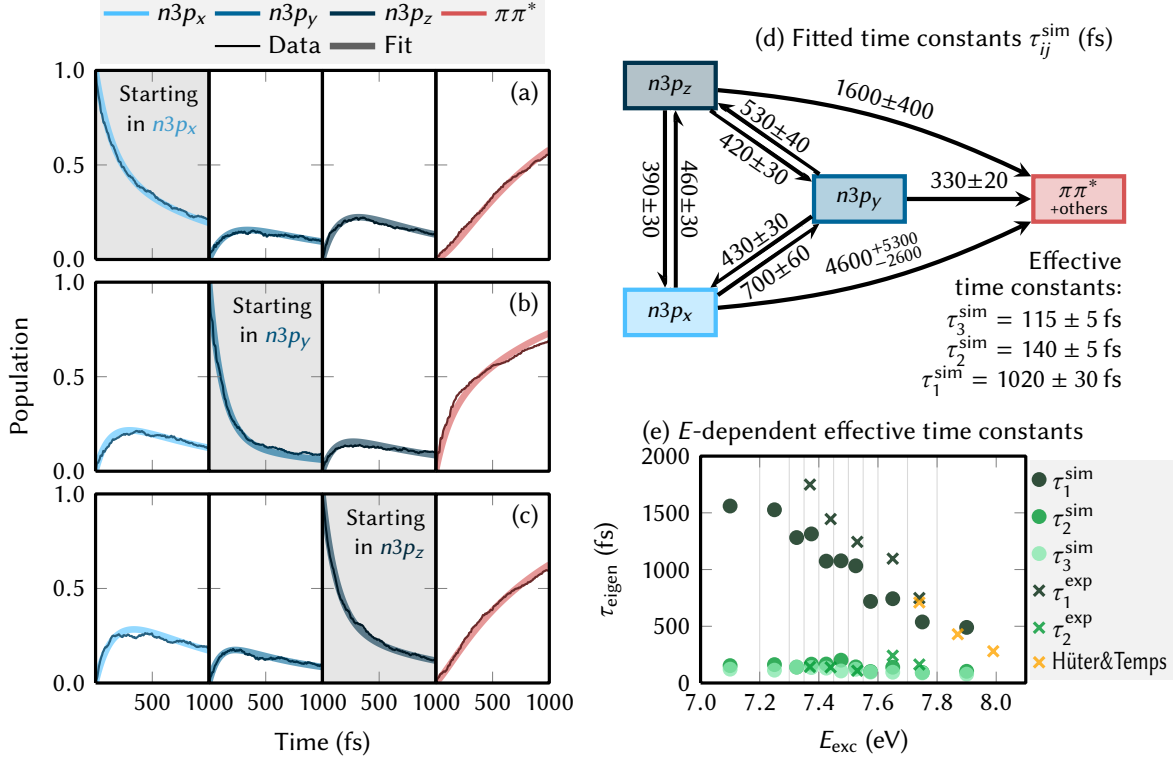
Figure 3: Overview of the theoretical results obtained with the SHARC-LVC method. (a)–(c) Temporal evolution of the diabatic populations (thin lines) and kinetic model fits (thick lines), for the ensemble starting in the (a) n3p$_x$, (b) n3p$_y$, and (c) n3p$_z$. (d) Scheme showing the fitted time constants and associated errors (see Figure S8 in Section S4 in the SI for a similar fit enforcing detailed balance, showing that $\tau_{xy}$ might be overestimated and $\tau_{xz}$ underestimated but otherwise the time constants are consistent with detailed balance). (e) Plot of the energy dependence of the eigenvalue-derived effective time constants and comparison to the experimental and literature [27] values.

in the SI) three independent ensembles of about 1000 trajectories each, in which the initial electronic wave function was, respectively, the pure n3p$_x$, n3p$_y$, or n3p$_z$ state. For each ensemble we monitored the population of the n3p$_x$, n3p$_y$, n3p$_z$, and $\pi\pi^*$ states, resulting in a set of twelve population transients. This strategy of simulating the decay of each initial state separately is essential, since there are nine independent time constants to fit and employing only four population transients (from a single ensemble) would lead to severe overfitting.

Fitted population transients are presented in Fig. 3. Panels (a) to (c) show the temporal evolution of the 12 population transients together with the fitting functions; the kinetic model fits the data excellently, with almost no systematic deviations. The obtained time

constants, which are shown in Fig. 3(d) together with their error estimates (obtained by bootstrapping), are quite interesting for the following three reasons: (i) The six inter-Rydberg time constants are relatively similar, with all constants ranging from 390 fs to 530 fs except $\tau_{xy}$ (700 fs). (ii) Population transfer towards energetically lower states proceeds faster ($\tau_{zx}$, $\tau_{zy}$, $\tau_{yx}$) than vice versa ($\tau_{xz}$, $\tau_{yz}$, $\tau_{xy}$). (iii) According to the three Rydberg decay constants, the n3p$_y$ state decays the fastest among the n3p states (5 and 13 times faster than n3p$_z$ and n3p$_x$, respectively), as previously suggested in the literature.[33–37] The time constants for the n3p$_z$ and n3p$_x$ states have large errors because the simulation time (1000 fs) is smaller than these estimated time constants. Especially the time constant for n3p$_x$ is extremely large and imprecise, which indicates that this time constant is not necessary to describe the population transients. As expected, the fastest decay occurs from the n3p$_y$ state to the $\pi\pi^*$ state, because both states have the same symmetry ($A_1$) and it is sufficient to accumulate energy in one of the totally symmetric modes that lead to an avoided crossing of these states. This situation is different from the decay between states of different symmetry, which requires accumulated energy in at least two normal modes—a totally symmetric tuning mode that makes the diabatic energies equal, and a non-symmetric coupling mode of the correct irreducible representation that induces some coupling between two states. The requirement of two activated normal modes explains why all population transfer processes between states of different symmetry are slower than the same-symmetry n3p$_y \rightarrow \pi\pi^*$ transfer. In general, the magnitude of the time constants suggests that in acetone the n3p Rydberg states readily interconvert among each other, due to their energetic closeness and the presence of coupling modes of all required symmetries.

In order to obtain information about the energy dependence of the relaxation time constants, we group all trajectories into eleven sub-ensembles based on their individual excitation energies. All fitted time constants are presented in Section S5 in the SI. The energy intervals and the corresponding effective time constants obtained are shown in Fig. 3e. The agreement of the energy dependence of the computed effective time constants with its

experimental counterpart is very good. The simulated values shown Fig. 3e confirm that there is one strongly energy-dependent effective time constant ($\tau_1$), being about 1600 fs for the lowest energies and about 500 fs for the highest ones. Additionally, there are two almost identical effective time constants ($\tau_2$, $\tau_3$) in the range of approximately 80 to 200 fs, only weakly depending on energy.

In conclusion, we demonstrate how a combination of TRPES with extensive surface hopping simulations is able to lift the veil that covers the details of nonadiabatic dynamics in energetically dense sets of states. Our synergistic approach allows disentangling the interconversion time scales among the three n3p states (n3p$_x$, n3p$_y$, and n3p$_z$) and the decay time scales to the dark $\pi\pi^*$ state in acetone. This work constitutes the first study that resolves the highly non-sequential population flow among these nearly degenerate states. An important key of accessing the individual time constants was the simulation of multiple independent ensembles with complementary initial conditions, as otherwise the global fit is severely under-determined. Despite the known limitations of trajectory surface-hopping methods,[40–42] the results of the simulations—validated through their good agreement with the experimental effective time constants and energy dependence, see also a simulated TRPES spectrum in Fig. S20 in the SI—show that the n3p$_y$ is most strongly coupled to the $\pi\pi^*$ state and exhibits the fastest decay, as expected from symmetry arguments. The n3p$_y$ also acts as the gateway state for the deactivation of the n3p$_x$ and n3p$_z$ states, as indicated by the fact that the n3p$_{x/z}$ $\rightarrow$ n3p$_y$ $\rightarrow$ $\pi\pi^*$ route is faster than the direct n3p$_{x/z}$ $\rightarrow$ $\pi\pi^*$ routes. The present results are expected to be helpful in understanding the light-driven dynamics of other aliphatic ketones and designing similar experiments. Further, they also evidence the power of using a linear vibronic coupling Hamiltonian within surface-hopping dynamics, as it allows considering large ensembles of trajectories propagating over a large number of electronic states.

# Methods

## Experimental

Pump-probe experiments were performed with femtosecond laser pulses from a commercial Ti:sapphire laser system with 800 nm central wavelength (for detail see Ref.[28]). Pump pulses were frequency up-converted by combining optical parametric amplification and subsequent frequency quadrupling to a wavelength range from 320 nm to 336 nm (6 nm, 15 meV full width at half maximum, FWHM). Probe pulses of 402 nm (3 nm, 60 meV FWHM) were obtained by frequency doubling with a BBO crystal. Dichroic mirrors were used in both beam paths to remove undesired wavelengths from the up-conversion process. The laser pulses were focused into the extraction region of a 0.5 m long, linear magnetic bottle time-of-flight spectrometer[43] where a small retarding field was used to increase the electron kinetic energy resolution. High purity acetone was introduced into the chamber as background gas with a partial pressure of about $4 \cdot 10^{-6}$ mbar.

## Computational

Potential energy surfaces of all electronic states of acetone were represented with a linear vibronic coupling (LVC) model[39,44] including all 24 vibrational degrees of freedom and 49 electronic states. This large number of states is necessary in order to include the important $\pi\pi^*$ state at the reference geometry ($S_{48}$). The reference harmonic potential was obtained from an optimization plus frequency calculation for the n3s state at the SOS-ADC(2) level of theory.[45] Parameters for the description of the excited-state potentials were obtained from calculations at the same level of theory. The basis set was a combination of cc-pVTZ[46] for C and O, cc-pVDZ[46] for H, and an additional $10s8p6d4f$ Rydberg basis set[47] at O. All electronic structure calculations were carried out with Turbomole 7.0.[48]

Initial conditions were sampled from the Wigner distribution of the SOS-ADC(2) harmonic oscillator of the ground state, generating 1000 initial geometries and velocities. Three

independent sets of trajectories were simulated from these, starting in either the n3p$_x$, n3p$_y$, and n3p$_z$ diabatic state. The trajectories were propagated with SHARC2.0[11,38] for 1000 fs using a 0.5 fs time step; the electronic coefficients were propagated with a 0.02 fs step using the local diabatization approach.[49] We applied an energy-based decoherence correction[50] and rescaled the full momentum vector during a hop.

The results were analyzed in terms of the diabatic state populations, to which the kinetic model was fitted. Additional analysis was carried out by dividing the set of trajectories into different energy windows and fitting their populations independently.

See the SI for additional computational details.

## Acknowledgement

## Supporting Information Available

Discussion and derivation of the fitting functions, experimental details regarding energy calibration, additional computational details, computational results, and supplementary files with all LVC parameters.

## References

(1) Herek, J. L.; Wohlleben, W.; Cogdell, R. J.; Zeidler, D.; Motzkus, M. Quantum control of energy flow in light harvesting. *Nature* **2002**, *417*, 533–535.

(2) Balzani, V.; Credi, A.; Venturi, M. Light powered molecular machines. *Chem. Soc. Rev.* **2009**, *38*, 1542–1550.

(3) Weinacht, T., Pearson, B. J., Eds. *Time-resolved spectroscopy: An experimental perspective*; CRC Press, 2019.

(4) Blanchet, V.; Zgierski, M. Z.; Seideman, T.; Stolow, A. Discerning vibronic molecular dynamics using time-resolved photoelectron spectroscopy. *Nature* **1999**, *401*, 52–54.

(5) Polli, D.; Altoe, P.; Weingart, O.; Spillane, K. M.; Manzoni, C.; Brida, D.; Tomasello, G.; Orlandi, G.; Kukura, P.; Mathies, R. A. et al. Conical intersection dynamics of the primary photoisomerization event in vision. *Nature* **2010**, *467*, 440–443.

(6) Schuurman, M. S.; Stolow, A. Dynamics at conical intersections. *Annu. Rev. Phys. Chem.* **2018**, *69*, 427–450.

(7) Timmers, H.; Zhu, X.; Li, Z.; Kobayashi, Y.; Sabbar, M.; Hollstein, M.; Reduzzi, M.; Martínez, T. J.; Neumark, D. M.; Leone, S. R. Disentangling conical intersection and coherent molecular dynamics in methyl bromide with attosecond transient absorption spectroscopy. *Nat. Commun.* **2019**, *10*, 3133.

(8) Garavelli, M. Computational organic photochemistry: Strategy, achievements and perspectives. *Theor. Chem. Acc.* **2006**, *116*, 87–105.

(9) Robb, M. A. *Theoretical chemistry for electronic excited states*; Theoretical and Computational Chemistry Series; The Royal Society of Chemistry, 2018; pp P001–225.

(10) Lasorne, B.; Worth, G. A.; Robb, M. A. Excited-state dynamics. *WIREs Comput. Mol. Sci.* **2011**, *1*, 460–475.

(11) Mai, S.; Marquetand, P.; González, L. Nonadiabatic dynamics: The SHARC approach. *WIREs Comput. Mol. Sci.* **2018**, *8*, e1370.

(12) Chergui, M. On the interplay between charge, spin and structural dynamics in transition metal complexes. *Dalton Trans.* **2012**, *41*, 13022–13029.

(13) Atkins, A. J.; González, L. Trajectory surface-hopping dynamics including intersystem crossing in $[Ru(bpy)_3]^{2+}$. *J. Phys. Chem. Lett.* **2017**, *8*, 3840–3845.

(14) Nogueira, J. J.; Plasser, F.; González, L. Electronic delocalization, charge transfer and hypochromism in the UV absorption spectrum of polyadenine unravelled by multiscale computations and quantitative wavefunction analysis. *Chem. Sci.* **2017**, *8*, 5682–5691.

(15) Koch, M.; Thaler, B.; Heim, P.; Ernst, W. E. The role of Rydberg-valence coupling in the ultrafast relaxation dynamics of acetone. *J. Phys. Chem. A* **2017**, *121*, 6398–6404.

(16) Nobre, M.; Fernandes, A.; da Silva, F. F.; Antunes, R.; Almeida, D.; Kokhan, V.; Hoffmann, S. V.; Mason, N.; Eden, S.; Limão-Vieira, P. The VUV electronic spectroscopy of acetone studied by synchrotron radiation. *Phys. Chem. Chem. Phys.* **2008**, *10*, 550–560.

(17) Holzapfel, W.; Finkele, U.; Kaiser, W.; Oesterhelt, D.; Scheer, H.; Stilz, H. U.; Zinth, W. Initial electron-transfer in the reaction center from Rhodobacter sphaeroides. *Proc. Natl. Acad. Sci.* **1990**, *87*, 5168–5172.

(18) van Stokkum, I. H.; Larsen, D. S.; van Grondelle, R. Global and target analysis of time-resolved spectra. *Biochem. Biophys. Acta Bioenergetics* **2004**, *1657*, 82 – 104.

(19) Wu, G.; Boguslavskiy, A. E.; Schalk, O.; Schuurman, M. S.; Stolow, A. Ultrafast non-adiabatic dynamics of methyl substituted ethylenes: The $\pi 3s$ Rydberg state. *J. Chem. Phys.* **2011**, *135*, 164309.

(20) Schalk, O.; Boguslavskiy, A. E.; Stolow, A. Substituent effects on dynamics at conical intersections: Cyclopentadienes. *J. Phys. Chem. A* **2010**, *114*, 4058–4064.

(21) Stolow, A.; Bragg, A. E.; Neumark, D. M. Femtosecond time-resolved photoelectron spectroscopy. *Chem. Rev.* **2004**, *104*, 1719–1758.

(22) Hertel, I. V.; Radloff, W. Ultrafast dynamics in isolated molecules and molecular clusters. *Rep. Prog. Phys.* **2006**, *69*, 1897.

(23) Kim, S. K.; Pedersen, S.; Zewail, A. H. Direct femtosecond observation of the transient intermediate in the $\alpha$-cleavage reaction of $(CH_3)_2CO$ to $2CH_3+CO$: Resolving the issue of concertedness. *J. Chem. Phys.* **1995**, *103*, 477.

(24) Shibata, T.; Suzuki, T. Photofragment ion imaging with femtosecond laser pulses. *Chem. Phys. Lett.* **1996**, *262*, 115–119.

(25) Buzza, S. A.; Snyder, E. M.; Castleman, A. W. Further direct evidence for stepwise dissociation of acetone and acetone clusters. *J. Chem. Phys.* **1996**, *104*, 5040.

(26) Rusteika, N.; Møller, K. B.; Sølling, T. I. New insights on the photodynamics of acetone excited with 253-288nm femtosecond pulses. *Chem. Phys. Lett.* **2008**, *461*, 193–197.

(27) Hüter, O.; Temps, F. Ultrafast $\alpha$–CC bond cleavage of acetone upon excitation to 3p and 3d Rydberg states by femtosecond time-resolved photoelectron imaging. *J. Chem. Phys.* **2016**, *145*, 214312.

(28) Maierhofer, P.; Bainschab, M.; Thaler, B.; Heim, P.; Ernst, W. E.; Koch, M. Disentangling multichannel photodissociation dynamics in acetone by time-resolved photoelectron-photoion coincidence spectroscopy. *J. Phys. Chem. A* **2016**, *120*, 6418–6423.

(29) Couch, D. E.; Kapteyn, H. C.; Murnane, M. M.; Peters, W. K. Uncovering highly-excited state mixing in acetone using ultrafast VUV pulses and coincidence imaging techniques. *J. Phys. Chem. A* **2017**, *121*, 2361–2366.

(30) Uenishi, R.; Horio, T.; Suzuki, T. Time-resolved photoelectron imaging of acetone with 9.3 eV photoexcitation. *J. Phys. Chem. A* **2019**, *123*, 6848–6853.

(31) Koch, M.; Heim, P.; Thaler, B.; Kitzler, M.; Ernst, W. E. Direct observation of a photochemical activation energy: a case study of acetone photodissociation. *J. Phys. B: At., Mol. Opt. Phys.* **2017**, *50*, 125102.

(32) Sølling, T. I.; Diau, E. W.-G.; Kötting, C.; De Feyter, S.; Zewail, A. H. Femtochemistry of Norrish Type I reactions: IV. Highly excited ketones—Experimental. *ChemPhysChem* **2002**, *3*, 79–97.

(33) Thakur, S. N.; Guo, D.; Kundu, T.; Goodman, L. Two-photon photoacoustic spectroscopy of acetone 3p Rydberg states. *Chem. Phys. Lett.* **1992**, *199*, 335–340.

(34) Xing, X.; McDiarmid, R.; Philis, J. G.; Goodman, L. Vibrational assignments in the 3p Rydberg states of acetone. *J. Chem. Phys.* **1993**, *99*, 7565–7573.

(35) Merchán, M.; Roos, B. O.; McDiarmid, R.; Xing, X. A combined theoretical and experimental determination of the electronic spectrum of acetone. *J. Chem. Phys.* **1996**, *104*, 1791.

(36) ter Steege, D. H. A.; Wirtz, A. C.; Buma, W. J. Vibronic coupling in excited states of acetone. *J. Chem. Phys.* **2002**, *116*, 547–560.

(37) McDiarmid, R.; Xing, X. Nonadiabatic coupling of the $3p$ Rydberg and $\pi\pi^*$ valence states of acetone. *J. Chem. Phys.* **1997**, *107*, 675–679.

(38) Mai, S.; Richter, M.; Heindl, M.; Menger, M. F. S. J.; Atkins, A. J.; Ruckenbauer, M.; Plasser, F.; Oppel, M.; Marquetand, P.; González, L. SHARC2.0: Surface Hopping Including Arbitrary Couplings – program package for non-adiabatic dynamics. sharc-md.org, 2018.

(39) Plasser, F.; Goméz, S.; Mai, S.; González, L. Highly efficient surface hopping dynamics using a linear vibronic coupling model. *Phys. Chem. Chem. Phys.* **2019**, *21*, 57–69.

(40) Subotnik, J. E.; Jain, A.; Landry, B.; Petit, A.; Ouyang, W.; Bellonzi, N. Understanding the surface hopping view of electronic transitions and decoherence. *Annu. Rev. Phys. Chem.* **2016**, *67*, 387–417.

(41) Wang, L.; Akimov, A.; Prezhdo, O. V. Recent progress in surface hopping: 2011–2015. *J. Phys. Chem. Lett.* **2016**, *7*, 2100–2112.

(42) Plasser, F.; Mai, S.; Fumanal, M.; Gindensperger, E.; Daniel, C.; González, L. Strong influence of decoherence corrections and momentum rescaling in surface hopping dynamics of transition metal complexes. *J. Chem. Theory Comput.* **2019**, *15*, 5031–5045.

(43) Kruit, P.; Read, F. Magnetic field paralleliser for $2\pi$ electron-spectrometer and electron-image magnifier. *J. Phys. E: Sci. Instrum.* **1983**, *16*, 313.

(44) Fumanal, M.; Plasser, F.; Mai, S.; Daniel, C.; Gindensperger, E. Interstate vibronic coupling constants between electronic excited states for complex molecules. *J. Chem. Phys.* **2018**, *148*, 124119.

(45) Dreuw, A.; Wormit, M. The algebraic diagrammatic construction scheme for the polarization propagator for the calculation of excited states. *WIREs Comput. Mol. Sci.* **2015**, *5*, 82–95.

(46) Dunning, T. H. Gaussian basis sets for use in correlated molecular calculations. I. The atoms boron through neon and hydrogen. *J. Chem. Phys.* **1989**, *90*, 1007–1023.

(47) Kaufmann, K.; Baumeister, W.; Jungen, M. Universal Gaussian basis sets for an optimum representation of Rydberg and continuum wavefunctions. *J. Phys. B: At. Mol. Phys.* **1989**, *22*, 2223.

(48) TURBOMOLE V7.0, A development of University of Karlsruhe and Forschungszentrum Karlsruhe GmbH. 2015.

(49) Granucci, G.; Persico, M.; Toniolo, A. Direct semiclassical simulation of photochemical processes with semiempirical wave functions. *J. Chem. Phys.* **2001**, *114*, 10608–10615.

(50) Granucci, G.; Persico, M. Critical appraisal of the fewest switches algorithm for surface hopping. *J. Chem. Phys.* **2007**, *126*, 134114.

# Supporting Information:
# Revealing Ultrafast Population Transfer Between Nearly Degenerated Electronic States

Pascal Heim,[†,§] Sebastian Mai,[‡,¶,§] Bernhard Thaler,[†] Stefan Cesnik,[†] Davide Avagliano,[‡] Dimitra Bella-Velidou,[‡] Wolfgang E. Ernst,[†] Leticia González,[*,‡] and Markus Koch[*,†]

†*Graz University of Technology, Institute of Experimental Physics, Petersgasse 16, A-8010 Graz, Austria*
‡*University of Vienna, Faculty of Vienna, Institute of Theoretical Chemistry, Währinger Str. 17, A-1090 Vienna, Austria*
¶*Present Address: Vienna University of Technology, Photonics Institute, Gußhausstr. 27–29, A-1040 Vienna, Austria*
§*These authors contributed equally to this work*

E-mail: leticia.gonzalez@univie.ac.at; markus.koch@tugraz.at

## Contents

# S1 Kinetic Model

We describe the population dynamics by the following differential equation system of a unimolecular first-order kinetic model:

$$\frac{\partial}{\partial t}\vec{P} = \mathbf{M}\vec{P} + g(t)\vec{P}_0, \tag{1}$$

with the time-dependent population vector $\vec{P}$:

$$\vec{P} = \begin{pmatrix} P_{\text{n3p}_\text{x}}(t) \\ P_{\text{n3p}_\text{y}}(t) \\ P_{\text{n3p}_\text{z}}(t) \\ P_{\pi\pi^*}(t) \end{pmatrix} \tag{2}$$

where $P_{\pi\pi^*}(t)$ also includes other dark states besides the $\pi\pi^*$. The coupling matrix $\mathbf{M}$ is:

$$\mathbf{M} = \begin{pmatrix} -\frac{1}{\tau_{\text{xy}}} - \frac{1}{\tau_{\text{xz}}} - \frac{1}{\tau_{\text{x}\pi}} & +\frac{1}{\tau_{\text{yx}}} & +\frac{1}{\tau_{\text{zx}}} & 0 \\ +\frac{1}{\tau_{\text{xy}}} & -\frac{1}{\tau_{\text{yx}}} - \frac{1}{\tau_{\text{yz}}} - \frac{1}{\tau_{\text{y}\pi}} & +\frac{1}{\tau_{\text{zy}}} & 0 \\ +\frac{1}{\tau_{\text{xz}}} & +\frac{1}{\tau_{\text{yz}}} & -\frac{1}{\tau_{\text{zx}}} - \frac{1}{\tau_{\text{zy}}} - \frac{1}{\tau_{\text{z}\pi}} & 0 \\ +\frac{1}{\tau_{\text{x}\pi}} & +\frac{1}{\tau_{\text{y}\pi}} & +\frac{1}{\tau_{\text{z}\pi}} & 0 \end{pmatrix}. \tag{3}$$

This matrix assumes that the n3p states couple to each other and decay to the $\pi\pi^*$ state, but we neglect population transfer from the $\pi\pi^*$ back to the n3p states. The term $g(t)\vec{P}_0$ in equation (1) is the source term that populates the states. It is the product of the normalized temporal profile of the laser excitation $g(t)$ and a state-dependent prefactor $\vec{P}_0$ that depends on the relevant transition dipole moments.

Equation (1) can be solved by convolution of the impulse response function of the linear differential equation with the source term:

$$\vec{P}(t) = g(t) \circledast \left(\Theta(t)e^{\mathbf{M}t}\right) \cdot \vec{P}_0 \tag{4}$$

If the matrix $\mathbf{M}$ is diagonalizable, i.e., $\mathbf{M} = \mathbf{V}\mathbf{\Lambda}\mathbf{V}^{-1}$, one can rewrite this equation as:

$$\vec{P}(t) = g(t) \circledast \left(\Theta(t)\mathbf{V}e^{\mathbf{\Lambda}t}\mathbf{V}^{-1}\right) \cdot \vec{P}_0, \tag{5}$$

with the eigenvalue matrix $\hat{\Lambda} = \text{diag}(\lambda_1, \lambda_2, \cdots) = \text{diag}(\tau_1^{-1}, \tau_2^{-1}, \cdots)$. The latter equation can be rewritten for the population of a single state as:

$$P_i(t) = \sum_m \sum_n g(t) \circledast \left(\Theta(t)e^{\frac{t}{\tau_m}}\right) V_{im}V_{mn}^{-1}P_{0,n}. \tag{6}$$

We note here that the coupling matrix $\mathbf{M}$ might have complex eigenvalues. Below, for the fits of the experimental time-resolved photoelectron spectrum, only real time constants were fitted. For the theoretical results, where the full coupling matrix is available, in few cases the eigenvalues were found to be complex. However, the imaginary part in the time constants was generally small (below 10% of the real part), and hence was neglected.

## S1.1 Fitting function for experimental data

The measured signal $S(E, t)$ depends on the photoelectron energy $(E)$ and the time delay between pump and probe pulses $(t)$. It can be described[S1] as the sum over the products of the spectral shape

of each state $\sigma_i(E)$, which also includes the ionization cross section, and time dependent population $P_i$ of each state convoluted with the temporal shape of the probe pulse $g'(t)$:

$$S(E,t) = g'(t) \circledast \sum_i P_i(t)\sigma_i(E) \tag{7}$$

Inserting equation (6) into (7) and separating the time-dependent and time-independent parts lead to:

$$S(E,t) = \sum_m \underbrace{g'(t) \circledast g(t) \circledast \left(\Theta(t)e^{\lambda_m t}\right)}_{f_m(t)} \underbrace{\sum_i \sum_n V_{im} V_{mn}^{-1} P_{0,n} \sigma_i(E)}_{\mathrm{DAS}_m(E)} . \tag{8}$$

Equation (8) is the basis for the definition of the fitting function that we employed for the global 2D fit of the experimental time-resolved photoelectron spectra. We assume a Gaussian shape for the pump pulse $g(t)$ and the probe pulse $g'(t)$, therefore the convolution of the pump and the probe pulse is also a Gaussian function. The temporal width of the resulting Gaussian function $g(t) \circledast g'(t)$ was determined by the fit to be 50–90 fs, depending on the excitation photon energy. To account for a cross correlation signal around $t = 0$ fs, we also added a Gaussian function times a "cross correlation spectrum" (CCS).

$$S^{\mathrm{Gaussian}}(E,t) = G(t)\mathrm{CCS}(E) \tag{9}$$

The optimal maximum number of $m$ in equation (8) was found by varying the maximum number of $m$ until we obtained a satisfactory fit without overfitting. The best fit was obtained with $m = \{1,2\}$.

We note here that the decay associated spectrum (DAS) in equation (8) are in general very difficult to interpret, because they depend on the initial populations and on the eigenvectors of the coupling matrix. Hence, only in the special cases of purely sequential or parallel kinetic models,[S2] the DAS can be directly linked to the underlying spectra of the electronic states $\sigma_i(E)$. Opposite signs of different DAS at the same energy are indicative of population transfer from one state to another, but determining the amount of population flux is only possible in a purely sequential model, which is not applicable in our case. Therefore, a closer interpretation of our DAS is not possible.

## S2    Calibration of photoelectron spectra

We calibrate our photoelectron (PE) spectra based on the energy of the n3p$_z$ state, $E_{\mathrm{n3p_z}}$, as determined by high-resolution synchrotron measurements.[S3] The measured PE energy, $E_{\mathrm{PE}}$ is calculated from

$$E_{\mathrm{PE}} = \hbar\omega_{\mathrm{probe}} + E_{\mathrm{n3pz}} - E_{\mathrm{IP}},$$

where $\hbar\omega_{\mathrm{probe}}$ is the probe photon energy and $E_{\mathrm{IP}}$ is the adiabatic acetone ionization potential ($E_{\mathrm{IP}}$=9.708 eV[S3]). This is necessary because the retarding voltage applied to increase the energy resolution causes some uncertainty of the measured PE kinetic energy, which depends on the exact potential at the location of ionization. Our calibration assumes that the potential energy surfaces of the excited and ionic states are parallel. Therefore we take the n3p$_z$ state as reference, since the n3p$_y$ is distorted due to coupling to the $\pi\pi^*$ state and the n3p$_x$ is populated in high vibrational states.

# S3   Additional Experimental Results

In the following, we present the experimental results for different excitation wavelengths from 320 nm to 336 nm. We show the transient photoelectron spectra, the 2D global fit with two time constants and Gaussian cross correlation function, the corresponding DAS, and the residua of the fit.
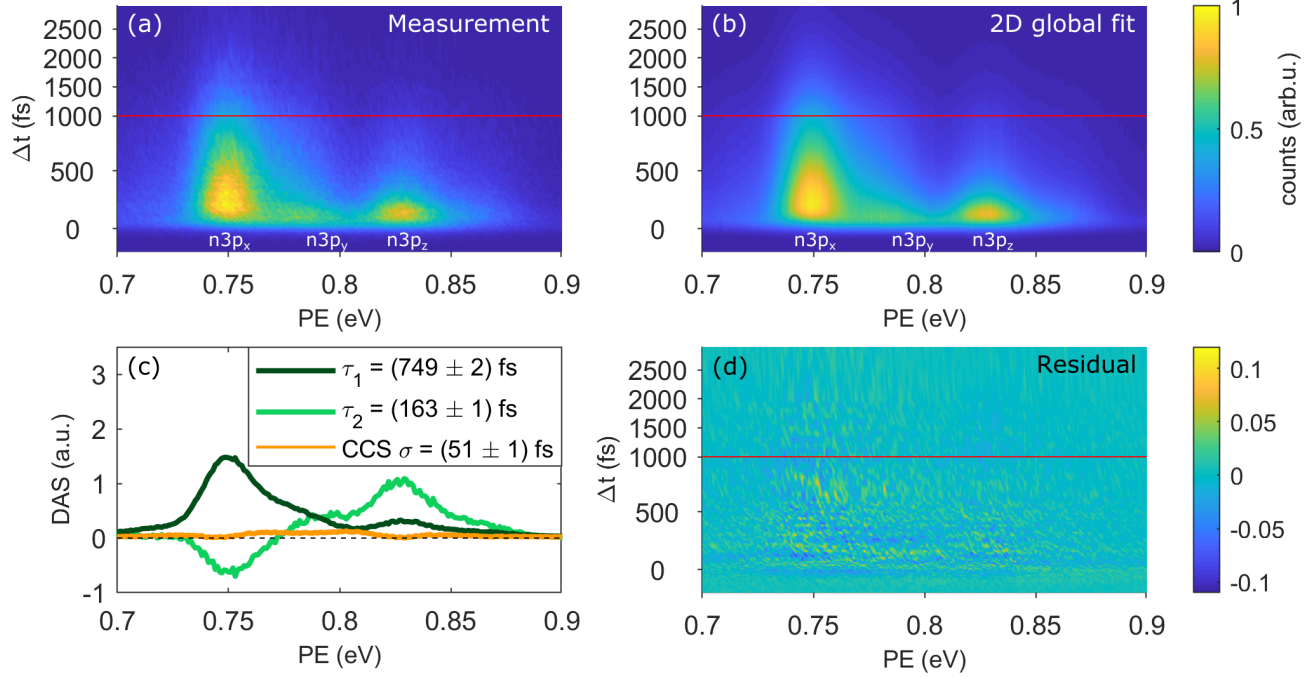


Figure S1: Measured photoelectron spectrum (a), its 2D global fit (b) with the corresponding DAS time constants and CCS with standard deviation of the Gaussian cross-correlation function (c) and residuals (d). Excitation wavelength is 320 nm. The red lines in (a), (b) and (c) indicate a change of the vertical scale.
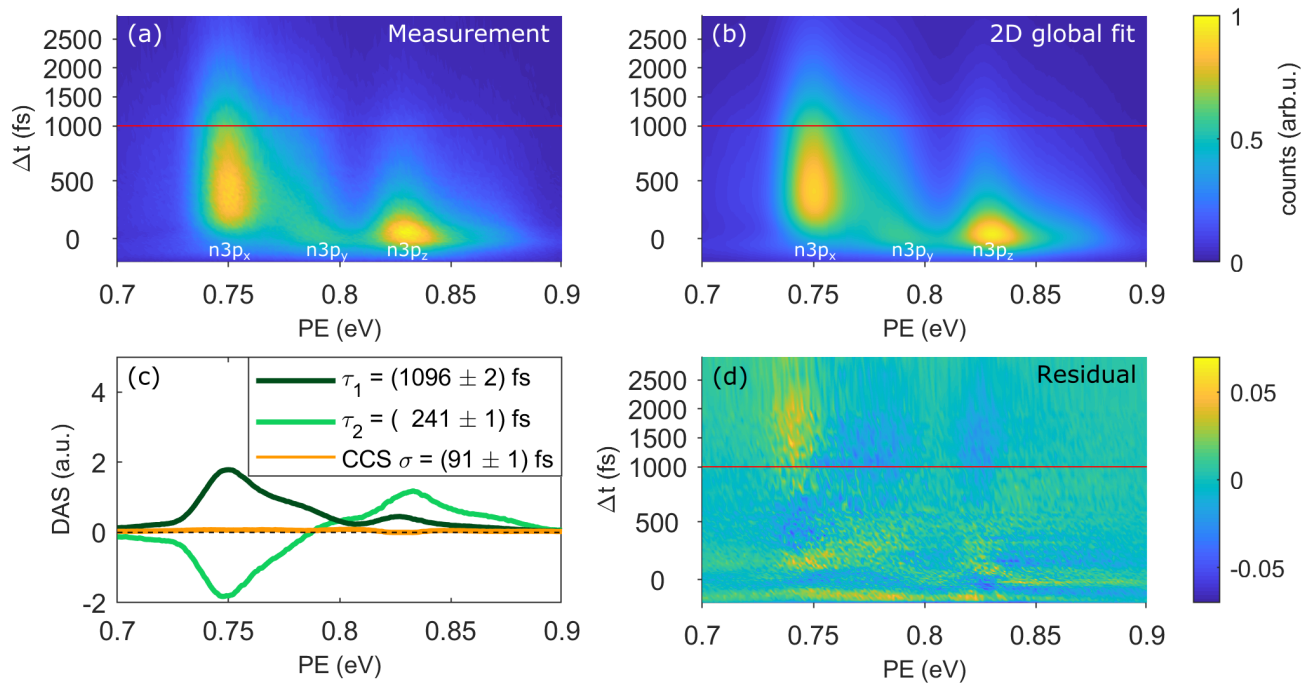
Figure S2: Measured photoelectron spectrum (a), its 2D global fit (b) with the corresponding DAS time constants and CCS with standard deviation of the Gaussian cross-correlation function (c) and residuals (d). Excitation wavelength is 324 nm. The red lines in (a), (b) and (c) indicate a change of the vertical scale.
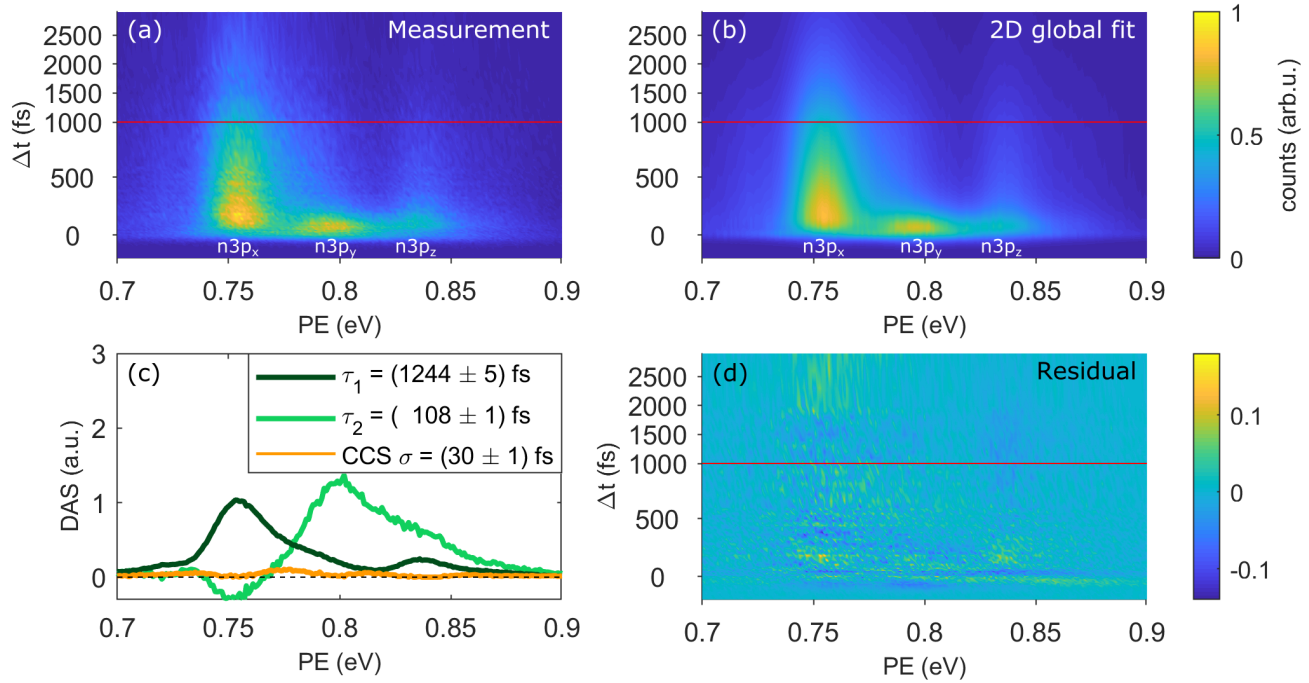


Figure S3: Measured photoelectron spectrum (a), its 2D global fit (b) with the corresponding DAS time constants and CCS with standard deviation of the Gaussian cross-correlation function (c) and residuals (d). Excitation wavelength is 329 nm. The red lines in (a), (b) and (c) indicate a change of the vertical scale.

Figure S4: Measured photoelectron spectrum (a), its 2D global fit (b) with the corresponding DAS time constants and CCS with standard deviation of the Gaussian cross-correlation function (c) and residuals (d). Excitation wavelength is 333 nm. The red lines in (a), (b) and (c) indicate a change of the vertical scale.
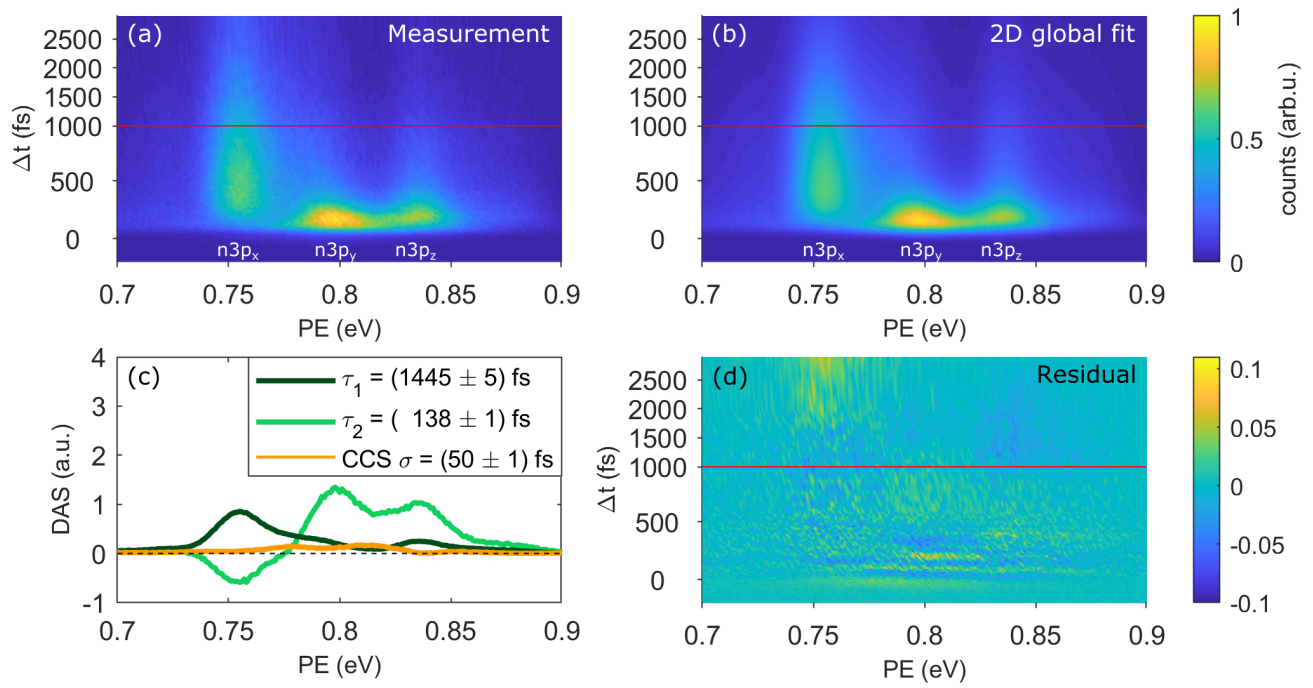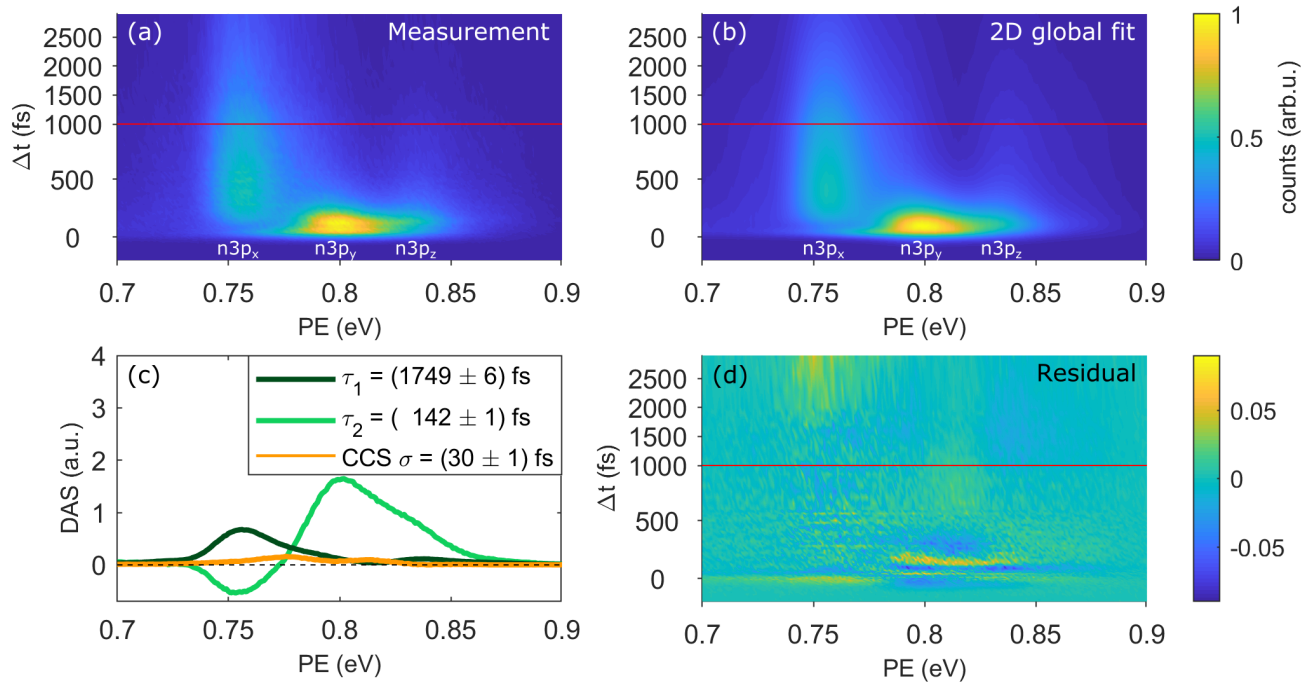


Figure S5: Measured photoelectron spectrum (a), its 2D global fit (b) with the corresponding DAS time constants and CCS with standard deviation of the Gaussian cross-correlation function (c) and residuals (d). Excitation wavelength is 336 nm. The red lines in (a), (b) and (c) indicate a change of the vertical scale.

# S4 Computational Details

## S4.1 The linear vibronic coupling model

In this work, we employ a linear vibronic coupling (LVC) model[S4,S5] to describe the coupled potential energy surfaces of the electronic states of acetone. An LVC model is a Taylor expansion of the potential energy surfaces around a reference geometry (e.g., the minimum of a representative state), expanded in normal mode coordinates. The mass-frequency-weighted normal mode coordinate $Q_i$ of mode $i$ is defined (in atomic units) as:

$$Q_i = \sqrt{\omega_i} \sum_A^{\text{atoms}} K_{Ai} \sqrt{M_A}(R_A - R_A^{\text{ref}}), \tag{10}$$

where $\omega_i$ is the normal-mode frequency, $K_{Ai}$ are elements of the Cartesian-normal mode transformation matrix, $M_A$ are the atomic masses, and $R_A$ are the Cartesian coordinates of the molecule.

The matrix of the electronic Hamiltonian is given by:

$$\mathbf{H}(\vec{Q}) = \mathbf{1}V_0(\vec{Q}) + \mathbf{W}(\vec{Q}). \tag{11}$$

The reference potential $V_0$ is identical for all electronic states, and in the present work given by the harmonic potential

$$V_0(\vec{Q}) = \sum_i^{\text{modes}} \frac{\omega_i}{2} Q_i^2. \tag{12}$$

The coupling matrix $\mathbf{W}(\vec{Q})$ serves to create the individual potential energy surfaces from the reference potential, and consists of constant and linear terms:

$$W_{\alpha\alpha}(\vec{Q}) = \epsilon_\alpha + \sum_i^{\text{modes}} \kappa_i^\alpha Q_i \tag{13}$$

and

$$W_{\alpha\beta}(\vec{Q}) = \sum_i^{\text{modes}} \lambda_i^{\alpha\beta} Q_i, \tag{14}$$

where $\epsilon_\alpha$ are the excitation energies at the reference geometry, $\kappa_i^\alpha$ are the gradients at the reference geometry, and $\lambda_i^{\alpha\beta}$ are the linear intrastate coupling constants. In this way, the Hamiltonian matrix $\mathbf{H}(\vec{Q})$ is given in a diabatic representation; a diagonalization of $\mathbf{H}(\vec{Q})$ then produces the adiabatic potential energy surfaces that we are employing for our dynamics simulations.

## S4.2 Electronic structure calculations

In order to find the parameter values for the LVC model, we employed the spin-opposite scaling variant of the algebraic diagrammatic construction scheme for the polarization propagator to second order (SOS-ADC(2)) method.[S6] The basis set, which needs to be able to describe a large set of high-lying Rydberg orbitals, was cc-pVTZ[S7] for O and C, cc-pVDZ[S7] for H, and an additional $10s8p6d4f$ Rydberg basis set[S8] centered on the O atom. All electronic structure calculations were carried out with Turbomole 7.0.[S9] Wave function overlaps between ADC(2) wave functions, needed to obtain the $\lambda$ parameters,[S10] were computed with the WFoverlap code.[S11] The molecule was oriented such that the $z$ axis is parallel to the molecular axis and the $x$ axis perpendicular to the molecular plane.

## S4.3    Parametrization of LVC model

The reference potential $V_0$ is fully specified with the masses $M_A$ and the parameters $\omega_i$ and $K_{Ai}$. These were obtained from a frequency calculation for the $n3s$ state at the SOS-ADC(2) level of theory. The $n3s$ state was chosen as it is well separated from other states and hence easy to optimize, but also parallel to the higher Rydberg states and therefore a better reference state than the $S_0$. We used all 24 normal modes of acetone (resulting in 720 $K_{Ai}$ elements and 24 $\omega_i$ parameters). An overview over the modes and the values of $\omega_i$ are given in Table S1.

The $\epsilon$ and $\kappa$ parameters were obtained from a single-point calculation at the reference geometry ($n3s$ minimum). The $\epsilon$ parameters are the vertical excitation energies at that geometry, and the $\kappa$ parameters are the gradients of the states transformed into the normal-mode basis. To obtain the $\lambda$ parameters, we employed a numerical differentiation scheme[S10] that requires two extra calculations for each normal mode and the computation of wave function overlaps between the states at the reference geometry and the displaced geometries.

Our LVC model contains 49 singlet state, which is necessary to include the $\pi\pi^*$ state that is very high in energy at the reference geometry. Based on the numbers and symmetries of the states ($12A_1$, $11A_2$, $5B_1$, $21B_2$) and normal modes ($8a_1$, $4a_2$, $5b_1$, $7b_2$), this LVC model contains 49 $\epsilon$ parameters, 392 non-zero $\kappa$ parameters, and 7280 non-zero $\lambda$ parameters. See Table S2 for the $\epsilon$ values of all states, and Table S3 for the $\kappa$ parameters. All parameters can be found in the supplementary files.

**Table S1: Normal modes for the $n3s$ state at the SOS-ADC(2) level of theory.**

| Mode[a] | Character | Symmetry | $\omega$ (cm$^{-1}$) |
|---|---|---|---|
| 7 | Methyl rotation asym | $a_2$ | 50.3 |
| 8 | Methyl rotation sym | $b_1$ | 161.0 |
| 9 | CCC bend | $a_1$ | 324.3 |
| 10 | CCO bend inplane | $b_2$ | 359.0 |
| 11 | O=CCC bend out of plane | $b_1$ | 565.6 |
| 12 | C-C stretch sym | $a_1$ | 757.2 |
| 13 | Methyl wagging asym | $a_2$ | 887.9 |
| 14 | Methyl wagging in plane | $b_2$ | 939.5 |
| 15 | Methyl wagging out of plane | $b_1$ | 1072.7 |
| 16 | Methyl wagging sym + C=O stretch | $a_1$ | 1073.9 |
| 17 | C-C stretch asym | $b_2$ | 1143.7 |
| 18 | Methyl breath + C=O stretch | $a_1$ | 1234.4 |
| 19 | Methyl breath | $b_2$ | 1323.2 |
| 20 | Methyl breath sym | $a_1$ | 1422.9 |
| 21 | Methyl breath asym | $b_2$ | 1423.6 |
| 22 | Methyl scissoring asym | $a_2$ | 1431.9 |
| 23 | Methyl scissoring sym + C=O stretch | $a_1$ | 1440.2 |
| 24 | Methyl scissoring out of plane | $b_1$ | 1460.8 |
| 25 | C-H stretch | $b_2$ | 2952.9 |
| 26 | C-H stretch | $a_1$ | 2961.7 |
| 27 | C-H stretch | $a_2$ | 3056.5 |
| 28 | C-H stretch | $b_1$ | 3118.2 |
| 29 | C-H stretch | $a_1$ | 3160.1 |
| 30 | C-H stretch | $b_2$ | 3167.3 |

[a] Numbering includes translational and rotational degrees of freedom to be consistent with the supplementary files containing the $K_{Ai}$ and $\lambda$ parameters.

Table S2: Electronic states of acetone at the SOS-ADC(2) level of theory. State order-ing and energies refer to the $S_0$ minimum at MP2 level of theory. The $\epsilon$ parameters refer to the $n3s$ minimum at SOS-ADC(2) level of theory. The $\Delta E_{\mathrm{vert}}$ column provides the vertical excitation energies from the $S_0$ minimum.

| State | Character | Symmetry | $\epsilon$ (eV) | $\Delta E_{\mathrm{vert}}$ (eV) |
|---|---|---|---|---|
| $S_0$ | closed shell | $A_1$ | 0.00 | 0.00 |
| $S_1$ | $n\pi$ | $A_2$ | 4.23 | 4.52 |
| $S_2$ | $n3s$ | $B_2$ | 6.22 | 6.56 |
| $S_3$ | $n3p_x$ | $A_2$ | 7.05 | 7.37 |
| $S_4$ | $n3p_y$ | $A_1$ | 7.09[a] | 7.41 |
| $S_5$ | $n3p_z$ | $B_2$ | 7.15 | 7.45 |
| $S_6$ | $n3d_{x^2-y^2}$ | $B_2$ | 7.51 | 7.87 |
| $S_7$ | $n3d_{yz}$ | $A_1$ | 7.74 | 8.05 |
| $S_8$ | $n3d_{xz}$ | $A_2$ | 7.75 | 8.08 |
| $S_9$ | $n3d_{xy}$ | $B_1$ | 7.77 | 8.10 |
| $S_{10}$ | $n3d_{z^2}$ | $B_2$ | 7.79 | 8.11 |
| $S_{11}$ | $n4s$ | $B_2$ | 7.83 | 8.16 |
| $S_{12}$ | $n4p_x$ | $A_2$ | 8.02 | 8.35 |
| $S_{13}$ | $n4p_z$ | $B_2$ | 8.06 | 8.39 |
| $S_{14}$ | $n4p_y$ | $A_1$ | 8.07 | 8.40 |
| $S_{15}$ | $n4d_{x^2-y^2}$ | $B_2$ | 8.18 | 8.52 |
| $S_{16}$ | $n4d_{yz}$ | $A_1$ | 8.29 | 8.61 |
| $S_{17}$ | $n4d_{xz}$ | $A_2$ | 8.28 | 8.61 |
| $S_{18}$ | $n4d_{xy}$ | $B_1$ | 8.30 | 8.63 |
| $S_{19}$ | $n4d_{z^2}$ | $B_2$ | 8.31 | 8.64 |
| $S_{20}$ | $n5s$ | $B_2$ | 8.32 | 8.65 |
| $S_{21}$ | $n5p_x$ | $A_2$ | 8.40 | 8.73 |
| $S_{22}$ | $n5p_y$ | $A_1$ | 8.41 | 8.74 |
| $S_{23}$ | $n5p_z$ | $B_2$ | 8.42 | 8.75 |
| $S_{24}$ | $n4f$ | $A_2$ | 8.43 | 8.75 |
| $S_{25}$ | $n4f$ | $B_2$ | 8.43 | 8.75 |
| $S_{26}$ | $n4f$ | $A_1$ | 8.43 | 8.76 |
| $S_{27}$ | $n4f$ | $B_1$ | 8.44 | 8.77 |
| $S_{28}$ | $n4f$ | $A_1$ | 8.46 | 8.79 |
| $S_{29}$ | $n4f$ | $B_2$ | 8.48 | 8.80 |
| $S_{30}$ | $n4f$ | $A_2$ | 8.48 | 8.80 |
| $S_{31}$ | $n6s$ | $B_2$ | 8.50 | 8.83 |
| $S_{32}$ | $n\sigma$ | $B_2$ | 8.59 | 8.92 |
| $S_{33}$ | $n6p_x$ | $A_2$ | 8.61 | 8.95 |
| $S_{34}$ | $n6p_z$ | $B_2$ | 8.63 | 8.96 |
| $S_{35}$ | $n6p_y$ | $A_1$ | 8.62 | 8.96 |
| $S_{36}$ | $n5d_{xz}$ | $A_2$ | 8.64 | 8.98 |
| $S_{37}$ | $n5d_{yz}$ | $A_1$ | 8.65 | 8.98 |
| $S_{38}$ | $n5d_{xy}$ | $B_1$ | 8.66 | 8.99 |
| $S_{39}$ | $n5d_{x^2-y^2}$ | $B_2$ | 8.67 | 9.00 |
| $S_{40}$ | $n5d_{z^2}$ | $B_2$ | 8.68 | 9.01 |
| $S_{41}$ | ? | $B_2$ | 8.74 | 9.07 |
| $S_{42}$ | ? | $B_2$ | 8.83 | 9.17 |
| $S_{43}$ | $n7p_x$ | $A_2$ | 8.94 | 9.27 |
| $S_{44}$ | $n7p_z$ | $B_2$ | 8.98 | 9.31 |
| $S_{45}$ | ? | $B_1$ | 8.81 | 9.32 |
| $S_{46}$ | $n7p_y$ | $A_1$ | 9.01 | 9.34 |
| $S_{47}$ | ? | $B_2$ | 9.02 | 9.37 |
| $S_{48}$ | $\pi\pi^*$ | $A_1$ | 8.77 | 9.51 |

[a] This value was decreased manually (from 7.14 eV) to fit the experimental excitation energy of $n3p_y$.

**Table S3: All non-zero $\kappa$ parameters in the LVC model (meV). Note that for the reference state, $S_2$, all $\kappa$ values are zero.**

| State | Character | $\kappa_9$ | $\kappa_{12}$ | $\kappa_{16}$ | $\kappa_{18}$ | $\kappa_{20}$ | $\kappa_{23}$ | $\kappa_{26}$ | $\kappa_{29}$ |
|---|---|---|---|---|---|---|---|---|---|
| $S_0$ | closed shell | 52 | -39 | 78 | 37 | -40 | 218 | -17 | 9 |
| $S_1$ | $n\pi$ | -14 | -53 | 261 | -285 | -54 | -125 | -6 | 14 |
| $S_2$ | $n3s$ | 0 | 0 | 0 | 0 | 0 | 0 | 0 | 0 |
| $S_3$ | $n3p_x$ | -17 | -8 | 14 | -5 | -14 | 12 | -50 | 14 |
| $S_4$ | $n3p_y$ | -19 | -5 | 12 | -40 | -24 | 23 | -30 | 5 |
| $S_5$ | $n3p_z$ | -16 | -5 | 11 | -34 | 8 | 39 | -42 | 8 |
| $S_6$ | $n3d_{x^2-y^2}$ | -11 | 2 | -7 | -15 | -28 | -11 | -14 | 20 |
| $S_7$ | $n3d_{yz}$ | -22 | -7 | 15 | -34 | -2 | 32 | -35 | 17 |
| $S_8$ | $n3d_{xz}$ | -21 | -4 | 9 | -26 | -1 | 25 | -27 | 6 |
| $S_9$ | $n3d_{xy}$ | -20 | -5 | 14 | -29 | -13 | 17 | -39 | 11 |
| $S_{10}$ | $n3d_{z^2}$ | -23 | -4 | 13 | -35 | -7 | 26 | -35 | 10 |
| $S_{11}$ | $n4s$ | -23 | -4 | 14 | -38 | -4 | 19 | -31 | 20 |
| $S_{12}$ | $n4p_x$ | -20 | -3 | 18 | -33 | -10 | 13 | -39 | 10 |
| $S_{13}$ | $n4p_z$ | -21 | -4 | 17 | -43 | -4 | 21 | -38 | 9 |
| $S_{14}$ | $n4p_y$ | -20 | -3 | 23 | -49 | -13 | 13 | -31 | 7 |
| $S_{15}$ | $n4d_{x^2-y^2}$ | -18 | 0 | 12 | -36 | -16 | 4 | -27 | 14 |
| $S_{16}$ | $n4d_{yz}$ | -22 | -4 | 20 | -44 | -6 | 19 | -35 | 13 |
| $S_{17}$ | $n4d_{xz}$ | -22 | -3 | 14 | -40 | -4 | 17 | -30 | 8 |
| $S_{18}$ | $n4d_{xy}$ | -21 | -3 | 19 | -41 | -10 | 14 | -37 | 11 |
| $S_{19}$ | $n4d_{z^2}$ | -25 | -2 | 19 | -42 | -4 | 19 | -35 | 10 |
| $S_{20}$ | $n5s$ | -23 | -3 | 17 | -46 | -9 | 14 | -33 | 19 |
| $S_{21}$ | $n5p_x$ | -22 | -3 | 19 | -42 | -10 | 13 | -36 | 10 |
| $S_{22}$ | $n5p_y$ | -23 | -3 | 24 | -49 | -12 | 9 | -31 | 8 |
| $S_{23}$ | $n5p_z$ | -24 | -3 | 20 | -45 | -7 | 17 | -36 | 10 |
| $S_{24}$ | $n4f$ | -22 | -4 | 16 | -38 | -11 | 17 | -37 | 10 |
| $S_{25}$ | $n4f$ | -22 | -4 | 18 | -39 | -6 | 21 | -35 | 14 |
| $S_{26}$ | $n4f$ | -22 | -2 | 21 | -48 | -11 | 13 | -34 | 10 |
| $S_{27}$ | $n4f$ | -24 | -3 | 17 | -38 | -9 | 22 | -34 | 9 |
| $S_{28}$ | $n4f$ | -24 | -3 | 19 | -42 | -9 | 20 | -36 | 10 |
| $S_{29}$ | $n4f$ | -23 | -2 | 18 | -37 | -9 | 21 | -36 | 10 |
| $S_{30}$ | $n4f$ | -22 | -2 | 18 | -38 | -9 | 21 | -36 | 10 |
| $S_{31}$ | $n6s$ | -19 | 0 | 18 | -43 | -12 | 7 | -31 | 10 |
| $S_{32}$ | $n\sigma$ | -24 | -2 | 17 | -47 | -13 | 9 | -32 | 21 |
| $S_{33}$ | $n6p_x$ | -22 | -2 | 20 | -45 | -9 | 11 | -36 | 10 |
| $S_{34}$ | $n6p_z$ | -23 | -2 | 20 | -49 | -3 | 15 | -35 | 8 |
| $S_{35}$ | $n6p_y$ | -19 | 3 | 60 | -99 | -5 | -25 | -24 | 9 |
| $S_{36}$ | $n5d_{xz}$ | -22 | -2 | 14 | -39 | -4 | 17 | -29 | 7 |
| $S_{37}$ | $n5d_{yz}$ | -23 | -4 | 21 | -45 | -8 | 20 | -34 | 10 |
| $S_{38}$ | $n5d_{xy}$ | -20 | -3 | 18 | -41 | -9 | 14 | -38 | 11 |
| $S_{39}$ | $n5d_{x^2-y^2}$ | -23 | -2 | 21 | -50 | -9 | 11 | -33 | 16 |
| $S_{40}$ | $n5d_{z^2}$ | -24 | -2 | 19 | -44 | -8 | 18 | -35 | 10 |
| $S_{41}$ | ? | -22 | -1 | 23 | -50 | -7 | 10 | -34 | 11 |
| $S_{42}$ | ? | -20 | -1 | 20 | -47 | -7 | 9 | -32 | 10 |
| $S_{43}$ | $n7p_x$ | -21 | -2 | 20 | -39 | -10 | 14 | -37 | 10 |
| $S_{44}$ | $n7p_z$ | -20 | -1 | 17 | -40 | -4 | 12 | -30 | 8 |
| $S_{45}$ | ? | -37 | -24 | 328 | -446 | -59 | -358 | 22 | 1 |
| $S_{46}$ | $n7p_y$ | -18 | 1 | 56 | -90 | -6 | -21 | -24 | 12 |
| $S_{47}$ | ? | -23 | -3 | 12 | -44 | -20 | 5 | -33 | 20 |
| $S_{48}$ | $\pi\pi^*$ | 2 | 38 | 328 | -465 | 20 | -549[a] | 41 | -3 |

[a] This value was increased manually from -277 meV to fit the $\pi\pi^*$ potential energy surface to the SOS-ADC(2) one around the $\pi\pi^*/n3p$ intersections.

We note here that two parameters were modified. The $\epsilon$ parameter for $n3p_y$ was decreased from 7.14 eV to 7.09 eV (for $n3p_x$ and $n3p_z$, no corrections were necessary). This adjustment produces a vertical excitation energy from the $S_0$ minimum to the $n3p_y$ state of 7.41 eV (see Table S2), in very good agreement with the experimental value of 7.40 eV.[S3] Additionally, the $\kappa$ parameter for the $\pi\pi^*$ state and mode 23 was doubled from -519 meV to -1038 meV, in order to make the position of the intersections of $\pi\pi^*$ with the three $n3p$ states agree with the SOS-ADC(2) data.

Figure S6 shows—for a representative scan along the C=O bond length—a comparison between the diabatic LVC potential energy surfaces, the adiabatic LVC potentials that were used to actually run the SHARC simulations, and the reference SOS-ADC(2) potentials. It can be seen that the adiabatic LVC potentials (i.e., after diagonalization of the Hamiltonian including all $\lambda$ parameters) can faithfully reproduce the shape of the potentials, especially in the relevant region indicated by the grey box. Comparison of panels (a) and (b) also shows that inclusion of the $\lambda$ parameters leads to the creation of the avoided crossings and significantly affect the shape of some potentials, most notably the $\pi\pi^*$ one.
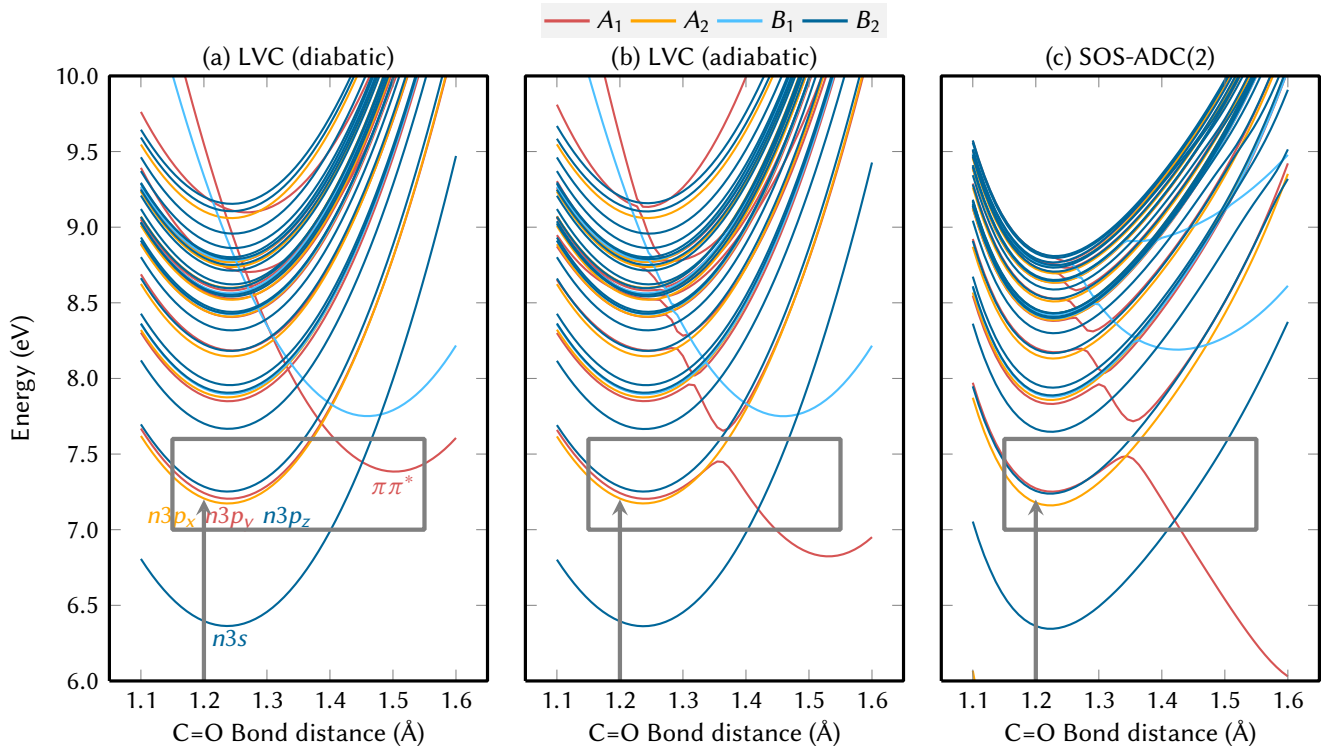


Figure S6: Comparison of potential energy surface scans along the C=O bond length of acetone. (a) shows the diabatic potentials from the LVC model (before including $\lambda$ parameters). (b) shows the adiabatic potentials from the LVC model after diagonalization. (c) shows the potentials from the SOS-ADC(2) method used for parametrization. Color indicates the irreducible representation of the states ($A_1$: red, $A_2$: orange, $B_1$: light black, $B_2$: dark black). The grey arrow indicates vertical excitation from the $S_0$ minimum, the grey box highlights the most relevant parts of the potentials. Note that in this diagram, 0 eV is the energy of $S_0$ at the n3s minimum and the minimum energy of $S_0$ is $-0.21$ eV.

## S4.4 Nonadiabatic dynamics simulations

A total of 1000 initial conditions were sampled from the Wigner distribution of the harmonic oscillator of the $S_0$ state, based on frequencies and normal modes computed at the SOS-MP2 level of theory with the basis set mentioned above. This sampling produced geometries in Cartesian coordinates, which were subsequently converted to the normal-mode basis of the $n3s$ state, in which the LVC model is defined.

To find the initial active states, we carried out a single point calculation with the LVC model for each of these 1000 geometries. In order to selectively excite into the $n3p_x$ Rydberg state, we set the diabatic transition dipole moment between $S_0$ and $n3p_x$ equal to one and all other transition dipole moments to zero for these single point calculations. Then, the initial active, adiabatic state was found stochastically[S12] in the excitation energy window from 6.77 eV to 8.27 eV. Hence, the initial active state was the adiabatic state that most resembled the $n3p_x$. The initial wave function coefficients were set such that the initial diabatic population of $n3p_x$ was 1. This procedure was then repeated to generate the initial conditions starting in the $n3p_y$ and $n3p_z$ states. The stochastic selection procedure accepted 947 initial conditions for the $n3p_x$ initial state, 929 for the $n3p_y$, and 921 for the $n3p_z$.

All 2797 initial conditions were then propagated for 1000 fs on the coupled 49 potential energy surfaces, using the PySHARC driver.[S5] The nuclear motion was propagated with a 0.5 fs step, and the electronic wave function was integrated with a 0.02 fs step, using the local diabatization scheme.[S13] The required wave function overlaps $\langle \Psi_i(t) | \Psi_j(t + \Delta t) \rangle$ were directly computed as the matrix product of the diabatic-adiabatic transformation matrices of both steps. During a hop, the full momentum vector was rescaled to conserve total energy. An energy-based decoherence correction[S14] (with the standard $\alpha$ parameter of 0.1 atomic units) was applied to the adiabatic wave function coefficients.

## S4.5 Electronic population analysis

The LVC model does not describe the minimum region of the $\pi\pi^*$ state fully accurately (see Figure S6), since the minimum is much too shallow. This inaccuracy could lead to trajectories crossing back from the $\pi\pi^*$ state to the Rydberg states. In order to avoid this artificial backflow, trajectories were scanned for hops from the $\pi\pi^*$ state to higher states and truncated to 10 fs before this backhop occurs. In this way, the $\pi\pi^*$ population is monotonically increasing, which is consistent with the expected behavior in the much deeper $\pi\pi^*$ potential energy surface described by SOS-ADC(2) (see Figure S6b).

The trajectory data was analyzed by means of the diabatic electronic populations. These were obtained by an adiabatic-diabatic transformation:

$$c_\alpha^{\text{diab}}(t_i) = \sum_\beta U_{\alpha\beta}(t_i) c_\beta^{\text{adiab}}(t_i), \tag{15}$$

with

$$\mathbf{U}(t_i) = \mathbf{T} \cdot \prod_{j=1}^{i} \mathbf{S}(t_{j-1}, t_j), \tag{16}$$

$$S_{\alpha\beta} = \left\langle \Psi_\alpha^{\text{adiab}}(t_{j-1}) \middle| \Psi_\beta^{\text{adiab}}(t_j) \right\rangle, \tag{17}$$

$$T_{\alpha\beta} = \left\langle \Psi_\alpha^{\text{diab}}(0) \middle| \Psi_\beta^{\text{adiab}}(0) \right\rangle, \tag{18}$$

where the matrix product in the first line was computed in a time-ordered fashion. This transfor-

mation yields for each trajectory $j$ the diabatic coefficients $c_{\alpha,j}^{\mathrm{diab}}(t_i)$, which are then incoherently averaged to give the total population of diabatic state $\alpha$:

$$P_\alpha^{\mathrm{diab}}(t_i) = \frac{1}{N_{\mathrm{traj}}} \sum_j^{N_{\mathrm{traj}}} \left| c_{\alpha,j}^{\mathrm{diab}}(t_i) \right|^2. \tag{19}$$

This averaging is independently done for each of the three ensembles (with initial state $n3p_x$, $n3p_y$, or $n3p_z$).

## S4.6  Fitting of the electronic populations

Since the diabatic model includes 49 electronic states, we obtain 49 population curves from the diabatization. However, only four states are appreciably populated: $n3p_x$, $n3p_y$, $n3p_z$, and $\pi\pi^*$. The other states are nevertheless necessary to improve the description of the potential energy surfaces of the n3p states of the more strongly coupled $\pi\pi^*$ state, but are generally weakly populated. Hence, to simplify the population analysis, the population of all remaining states is summed with the $\pi\pi^*$ state, and one single label is used.

The population data with $3 \times 4$ states was then fitted in a global procedure with the solution of equation (1). Because in the simulations, no explicit pump laser was used, the source term $g(t)$ is 1 at $t = 0$ and zero everywhere else. This simplifies equation (4) to:

$$\vec{P}(t) = e^{\mathbf{M}t} \cdot \vec{P}_0 \tag{20}$$

for $t \geq 0$. In accord with the employed initial conditions, the $\vec{P}_0$ vector was simply $P_0^{n3p_x} = (1,0,0,0)$, $P_0^{n3p_y} = (0,1,0,0)$, or $P_0^{n3p_z} = (0,0,1,0)$. For the actual fitting procedure, equation (20) was solved numerically with the Runge-Kutta 5(4) algorithm[S15] with suitable initial guesses for all time constants $(\tau_{xy}, \tau_{xz}, \tau_{yx}, \tau_{yz}, \tau_{zx}, \tau_{zy}, \tau_{x\pi}, \tau_{y\pi},$ and $\tau_{z\pi})$. The time constants were then optimized with the "Trust Region Reflective" algorithm[S16] implemented in SciPy, which was employed to restrain all time constants to be positive. By diagonalizing the coupling matrix $\mathbf{M}$ with the optimized time constants, we obtain the simulated eigenvalues $\lambda_m$, which can also be converted to the effective time constants by $\tau_m = \lambda_m^{-1}$.

To estimate the errors in the obtained time constants, we employed the bootstrapping method,[S17,S18] where we generated 1000 copies of the ensemble population data by random resampling with replacement (i.e., in the resamples some trajectories appear several times and others do not). These 1000 copies were fitted to the same kinetic model, yielding 1000 realizations of the time constants. From the histograms of these realizations, the fitting errors given in the manuscript were obtained as the arithmetic standard deviations (for $\tau_{x\pi}$, the multiplicative geometric standard deviation $\sigma_g$ is shown as $\mathrm{mean}_{\mathrm{mean}(\sigma_g^{-1}-1)}^{+\mathrm{mean}(\sigma_g-1)}$). To estimate the error in the time constants derived from the eigenvalues, the coupling matrix was diagonalized for each realization of the fitted time constants and the histograms of the resulting effective time constants analyzed.

## S4.7  Energy-dependent analysis

The sampling of the initial conditions from the Wigner distribution leads to a set of geometry snapshots with different kinetic and potential energies. On average, the kinetic and potential energy of the sampled ground state agrees with the zero-point energy, but each individual snapshot can have kinetic and/or potential energy above/below the zero-point energy. This distribution of energies is presented in Figure S7. Panel (a) shows the uncorrelated distribution of kinetic and potential
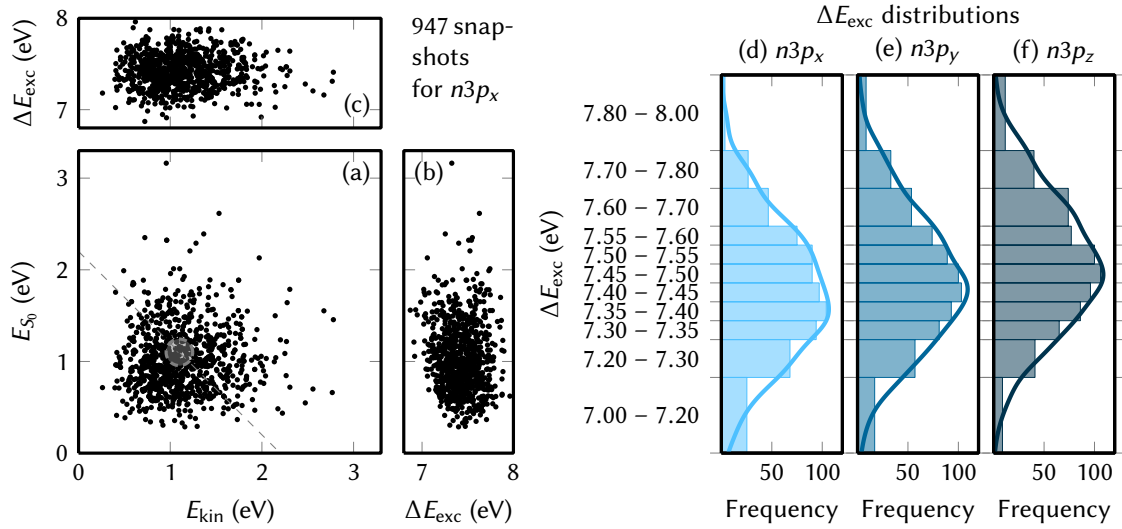
Figure S7: Plots of the distribution of energies in the initial condition snapshots. (a)–(c) Scatter plots of the kinetic energy $E_{\text{kin}}$, the ground state potential energy $E_{S_0}$, and the excitation energy $\Delta E_{\text{exc}}$ for the $n3p_x$ initial conditions, showing the spread of these energetic values. In (a), the dashed line and grey circle indicate the zero-point energy of about $2.2\,\text{eV}$. (d)–(f) Histograms of the distribution of excitation energy $\Delta E_{\text{exc}}$ of the initial conditions. The shown energy windows are the basis of the energy-resolved analysis of the population dynamics.

energy. Panels (b) and (c) also show the distribution of the excitation energies (exemplarily for $n3p_x$). The distributions of excitation energies for all three ensembles is shown in panels (d) to (f).

The rather broad distribution of excitation energies in the initial condition hampers the direct comparison of the full ensemble results with experiment because the latter excites only to a narrow window of excitation energy. Hence, the full ensemble results should be understood as average results, which should be compared to the average of the experimental results for different energies. However, the broad excitation distribution allows us to easily perform an energy-resolved analysis. For this analysis, the excitation energy was binned into 11 intervals (with 7.0–7.2 eV being the first one, and 7.8–8.0 eV the last one, see Figure S7d–f). For each of these intervals, the electronic populations were independently extracted and fitted according to the protocol presented above. Thus, the fitting protocol provides the 9 fitting parameters for each energy interval separately, allowing the observation of an energy-dependence of the time constants. Also for these time constants, we computed the effective time constants via diagonalization of the coupling matrix. Figures S9 to S19 present the global population fits for the individual energy ranges.

# S5 Additional Computational Results
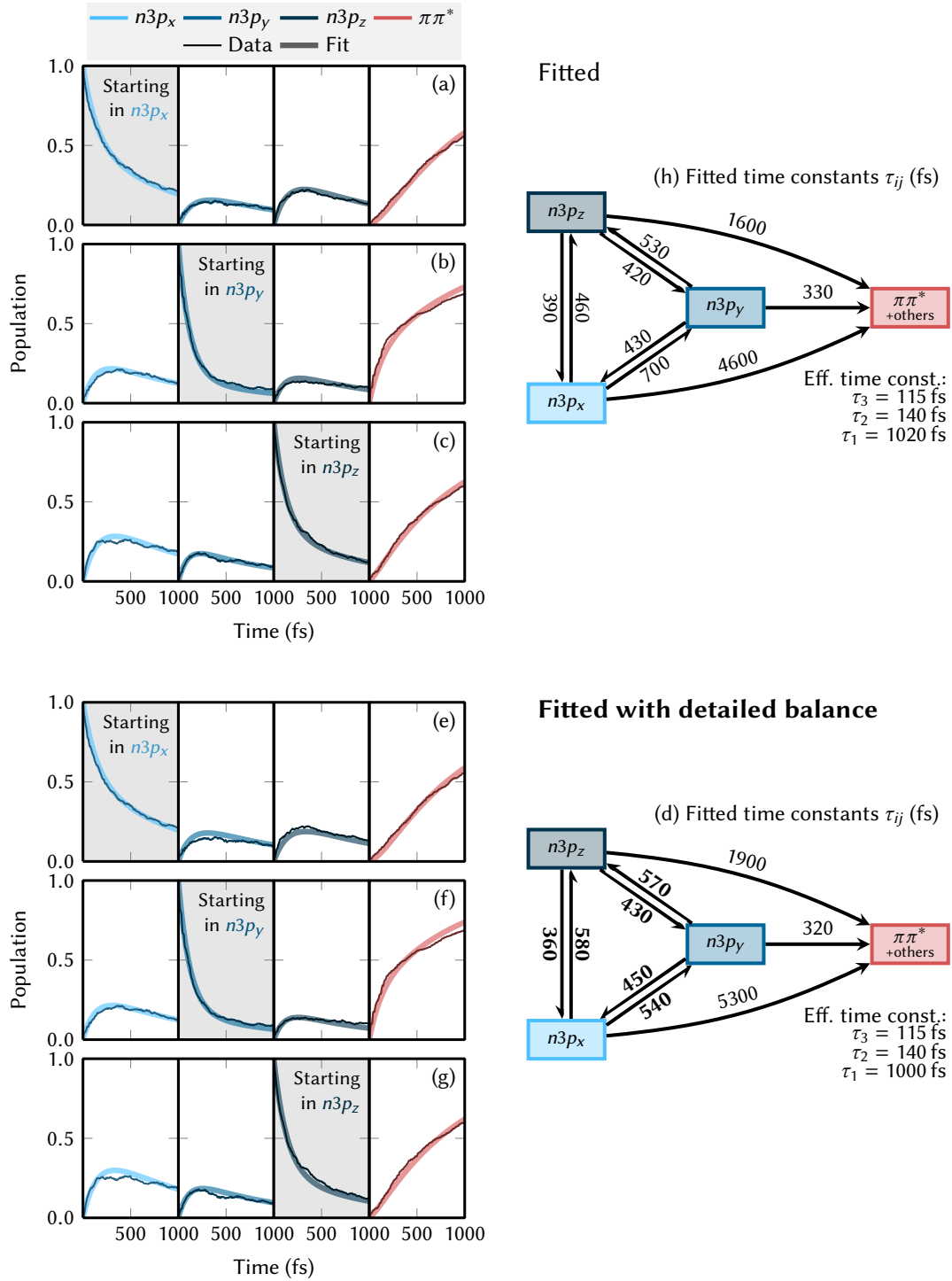


Figure S8: (a)–(d) Global fit of the electronic populations with nine independent time constants (identical with Figure 3). (e)–(h) Global fit with six independent time constants, where the ratios between back- and forth reactions (i.e., $\tau_{xy}/\tau_{yx}$, $\tau_{xz}/\tau_{zx}$, and $\tau_{yz}/\tau_{zy}$) were held constant at $\frac{\tau_{ij}}{\tau_{ji}} = \exp(-\frac{E_i - E_j}{k_B T_{\text{eff}}})$ ($T_{\text{eff}} = 2500 \, \text{K}$) such that the time constants obey detailed balance. The constrained fit is almost as good ($\chi^2 = 5.9$) as the unconstrained fit ($\chi^2 = 3.6$), and most time constants (except $\tau_{xy}$ and $\tau_{xz}$ are within the error estimate of the unconstrained fit.

Table S4 collects all obtained time constants for the full ensemble and for the different energy ranges. Table S5 gives the number of trajectories within each full ensemble and for the energy ranges.

**Table S4: Fitted time constants for the full ensemble with error estimates (from bootstrapping) and for the different energy ranges (all in fs). The sum of square residuals ($\chi^2$) are also given.**

| Energy range | $\tau_{xy}$ | $\tau_{xz}$ | $\tau_{yx}$ | $\tau_{yz}$ | $\tau_{zx}$ | $\tau_{zy}$ |
|---|---|---|---|---|---|---|
| Full ensemble | 701±56 | 455±30 | 430±29 | 533±43 | 395±28 | 417±26 |
| 7.0 − 7.2 eV | 1012 | 488 | 362 | 527 | 385 | 345 |
| 7.0 − 7.3 eV | 810 | 459 | 482 | 465 | 370 | 344 |
| 7.3 − 7.35 eV | 660 | 420 | 273 | 2252 | 408 | 581 |
| 7.35 − 7.4 eV | 698 | 583 | 472 | 664 | 418 | 477 |
| 7.4 − 7.45 eV | 607 | 647 | 589 | 540 | 434 | 414 |
| 7.45 − 7.5 eV | 917 | 703 | 570 | 433 | 645 | 389 |
| 7.5 − 7.55 eV | 1086 | 403 | 434 | 577 | 428 | 404 |
| 7.55 − 7.6 eV | 433 | 303 | 372 | 485 | 240 | 594 |
| 7.6 − 7.7 eV | 613 | 500 | 504 | 525 | 327 | 519 |
| 7.7 − 7.8 eV | 1037 | 261 | 370 | 479 | 298 | 287 |
| 7.8 − 8.0 eV | 1898 | 279 | 975 | 289 | 237 | 423 |

| Energy range | $\tau_{x\pi}$ | $\tau_{y\pi}$ | $\tau_{z\pi}$ | $\Re(\tau_1)$ | $\Re(\tau_2)$ | $\Re(\tau_3)$ | $\chi^2$ |
|---|---|---|---|---|---|---|---|
| Full ensemble | $4605^{+5266}_{-2600}$ | 329±22 | 1567±360 | 1015±26 | 142±6 | 116±4 | 3.63 |
| 7.0 − 7.2 eV | 2475 | 942 | 1454 | 1560 | 153 | 122 | 12.13 |
| 7.0 − 7.3 eV | ∞ | 762 | 891 | 1527 | 162 | 113 | 10.28 |
| 7.3 − 7.35 eV | 2581 | 512 | 2076 | 1282 | 140$^a$ | 140$^a$ | 13.86 |
| 7.35 − 7.4 eV | 3076 | 389 | ∞ | 1314 | 166 | 136 | 8.53 |
| 7.4 − 7.45 eV | 2285 | 417 | 4124 | 1074 | 167 | 131 | 9.63 |
| 7.45 − 7.5 eV | ∞ | 248 | 1756 | 1077 | 201 | 106 | 13.59 |
| 7.5 − 7.55 eV | 1584 | 300 | 20,061 | 1033 | 142 | 121 | 12.72 |
| 7.55 − 7.6 eV | 1761 | 239 | 1377 | 719 | 101 | 96 | 9.93 |
| 7.6 − 7.7 eV | 1892 | 172 | 4217 | 743 | 139 | 95 | 4.87 |
| 7.7 − 7.8 eV | 877 | 176 | 1532 | 538 | 93 | 89 | 9.95 |
| 7.8 − 8.0 eV | 378 | 150 | ∞ | 490 | 103 | 78 | 29.9 |

$^a$ Complex eigenvalues with small ($< 10\%$) imaginary components.

**Table S5: Number of trajectories in each ensemble and each energy range.**

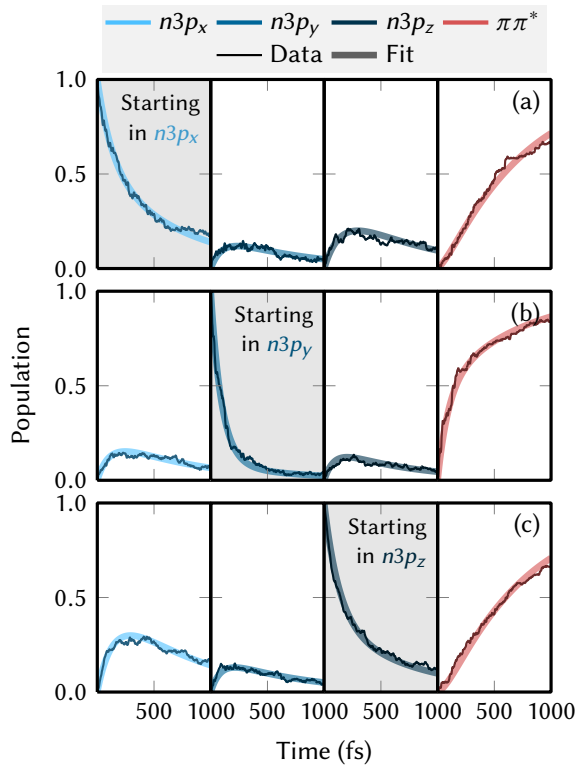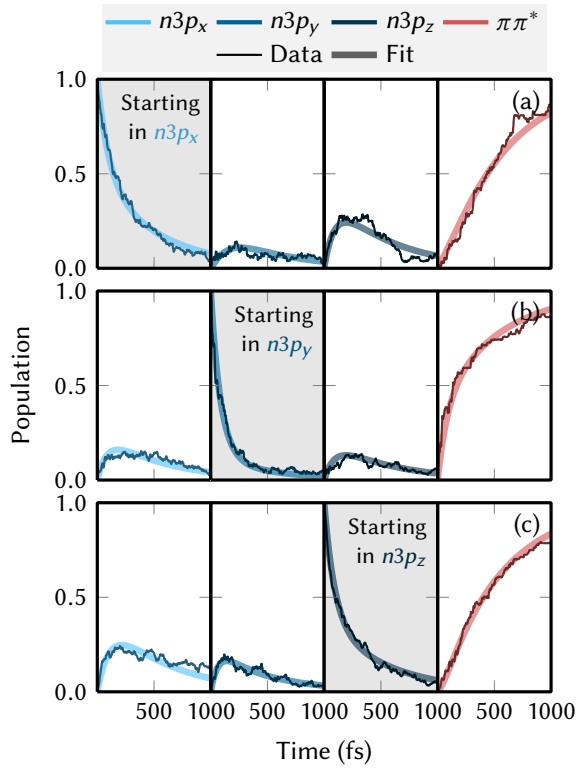| Energy range | $N_{n3p_x}^{\text{traj}}$ | $N_{n3p_y}^{\text{traj}}$ | $N_{n3p_z}^{\text{traj}}$ |
|---|---|---|---|
| Full ensemble | 947 | 929 | 921 |
| $7.0 - 7.2$ eV | 101 | 68 | 35 |
| $7.0 - 7.3$ eV | 136 | 114 | 82 |
| $7.3 - 7.35$ eV | 94 | 81 | 65 |
| $7.35 - 7.4$ eV | 104 | 93 | 86 |
| $7.4 - 7.45$ eV | 97 | 103 | 96 |
| $7.45 - 7.5$ eV | 90 | 100 | 106 |
| $7.5 - 7.55$ eV | 90 | 89 | 100 |
| $7.55 - 7.6$ eV | 75 | 74 | 77 |
| $7.6 - 7.7$ eV | 93 | 107 | 148 |
| $7.7 - 7.8$ eV | 53 | 66 | 80 |
| $7.8 - 8.0$ eV | 14 | 34 | 46 |
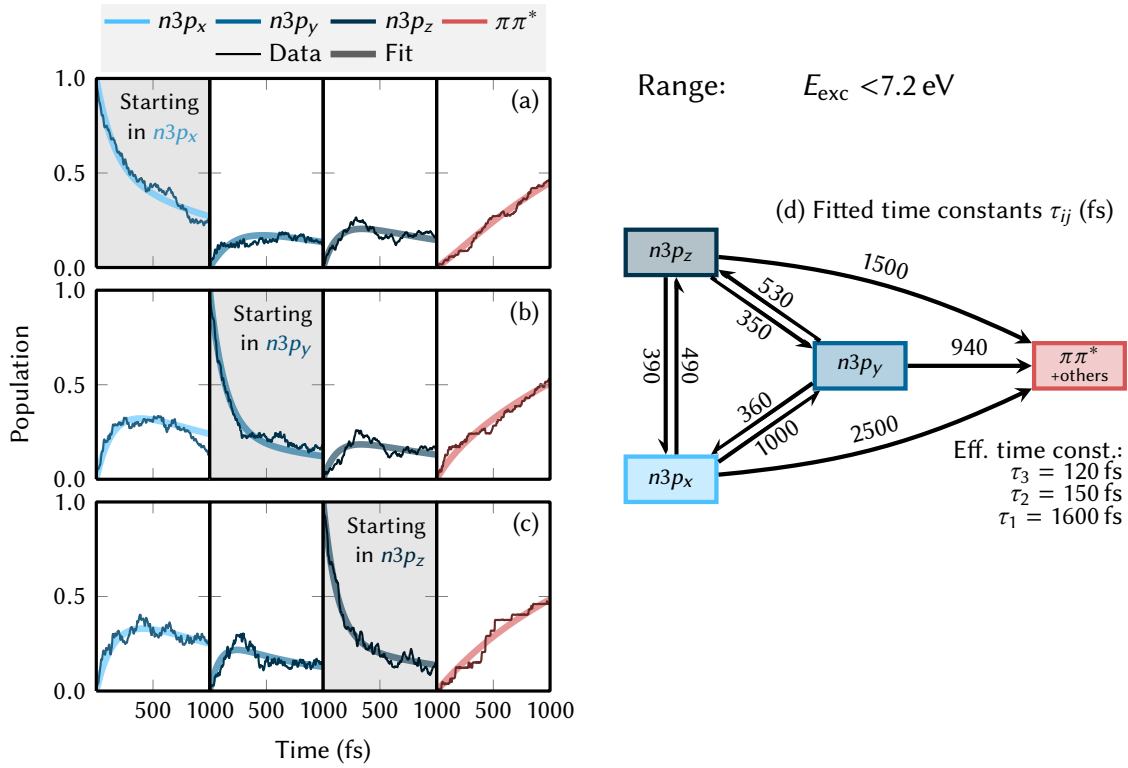


Figure S9: Results of the global fit of the electronic populations in the energy range 7.0–7.2 eV.
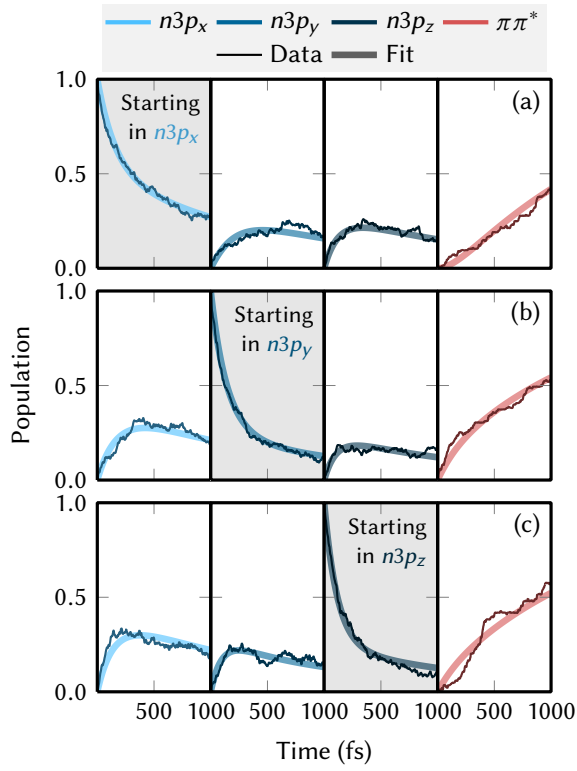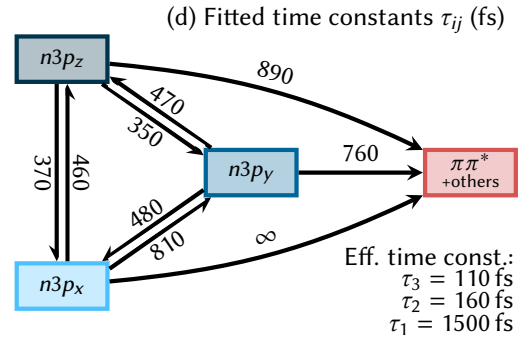
Figure S10: Results of the global fit of the electronic populations in the energy range 7.2–7.3 eV.
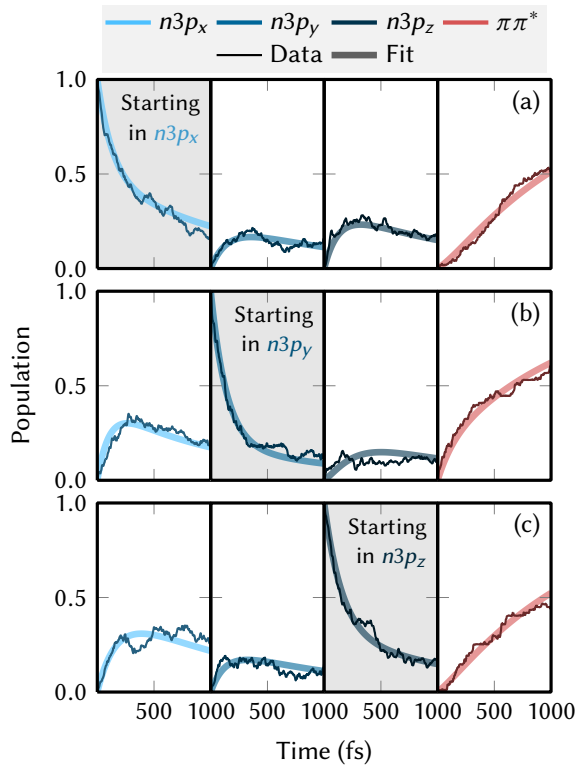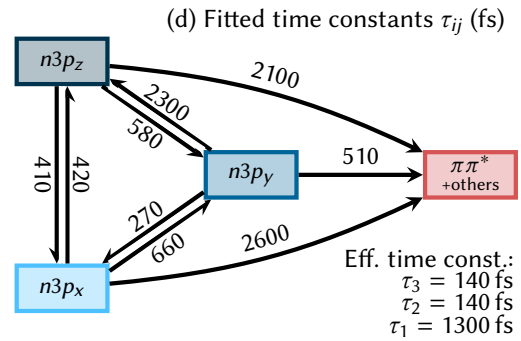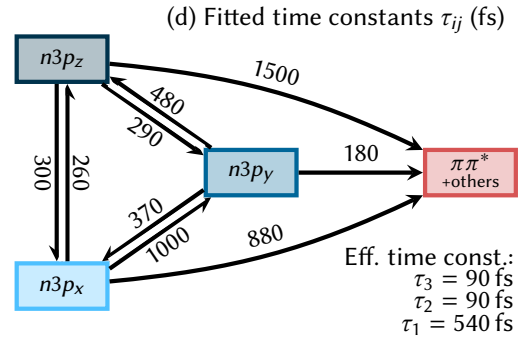


Figure S11: Results of the global fit of the electronic populations in the energy range 7.3–7.35 eV.
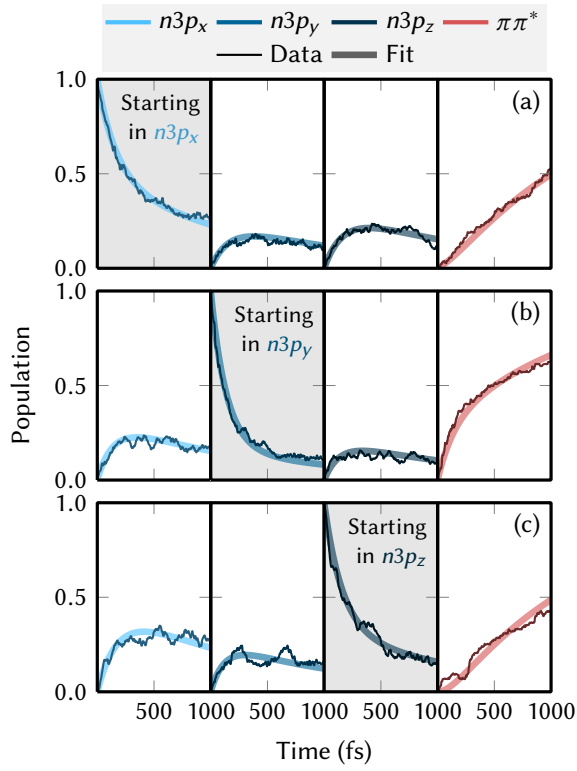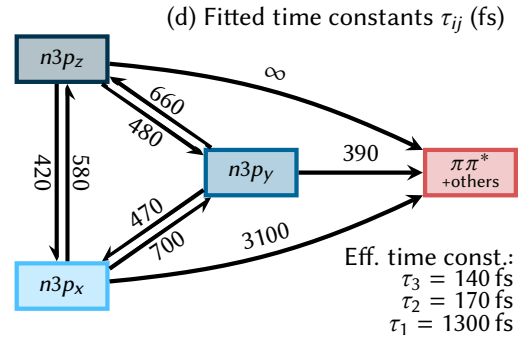
Figure S12: Results of the global fit of the electronic populations in the energy range 7.35–7.4 eV.
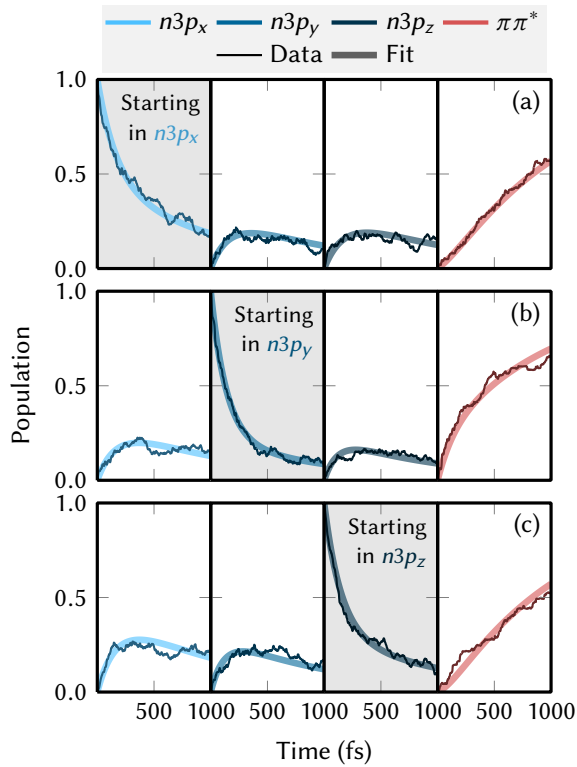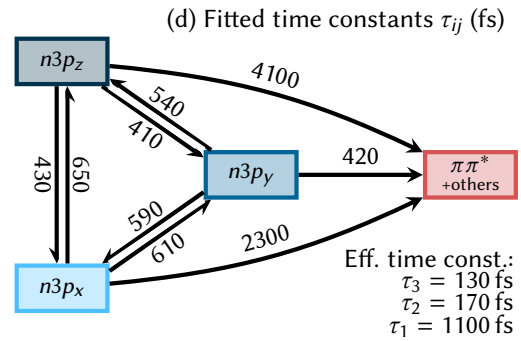


Figure S13: Results of the global fit of the electronic populations in the energy range 7.4–7.45 eV.
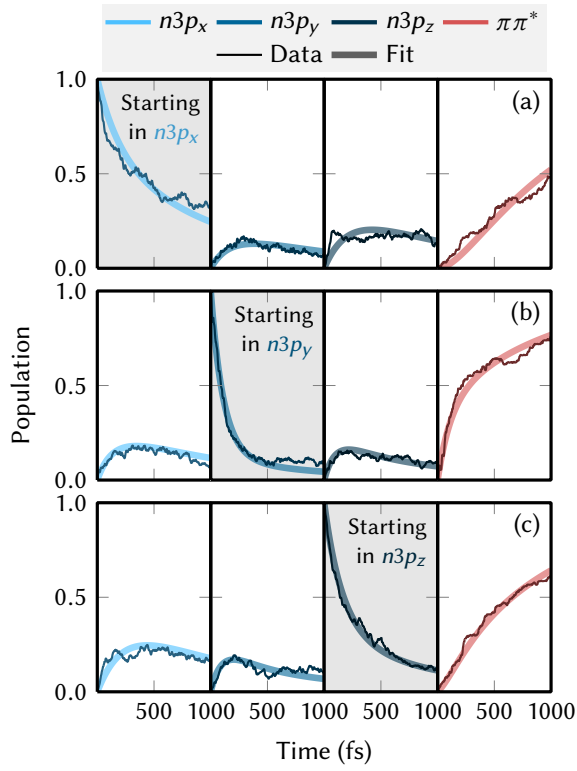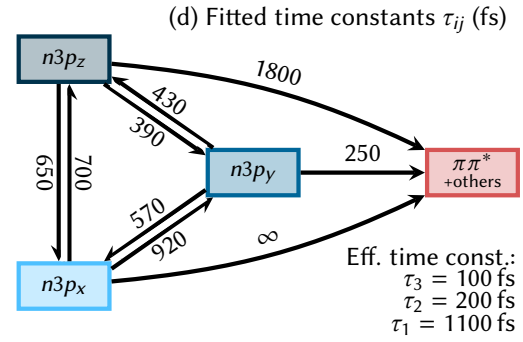
Figure S14: Results of the global fit of the electronic populations in the energy range 7.45–7.5 eV.
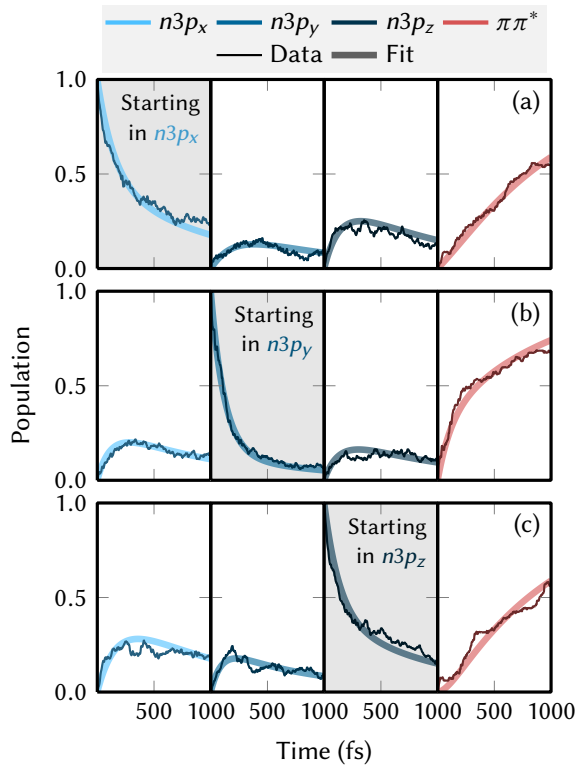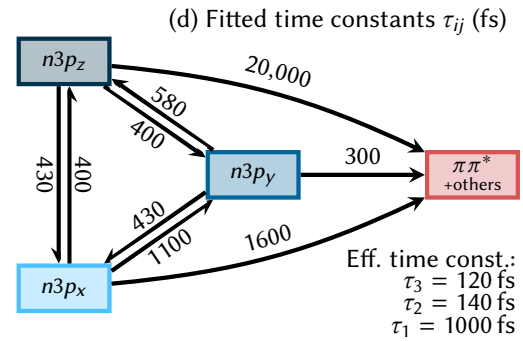


Figure S15: Results of the global fit of the electronic populations in the energy range 7.5–7.55 eV.
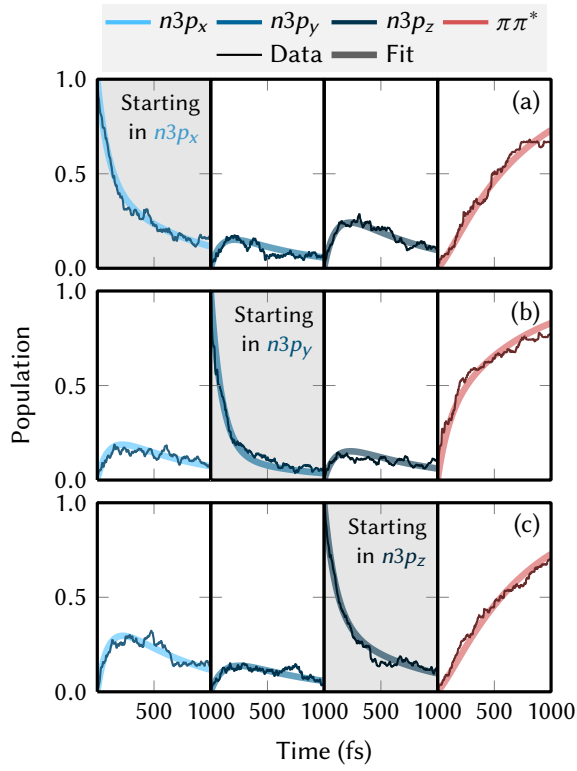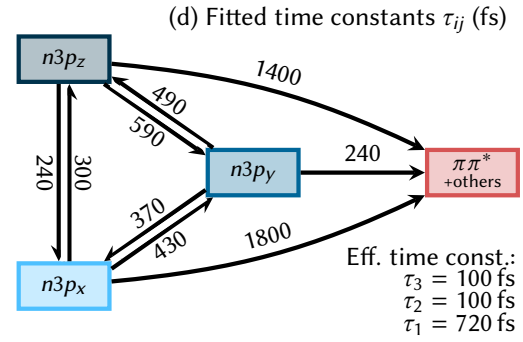
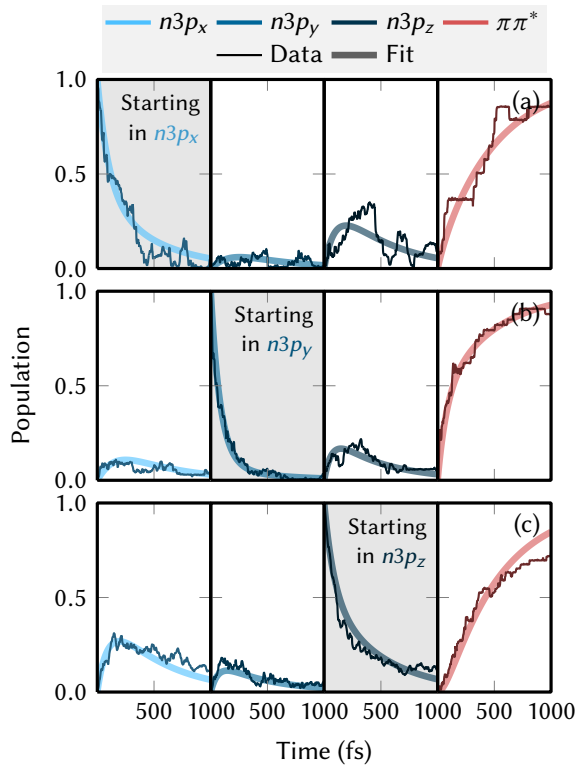Figure S16: Results of the global fit of the electronic populations in the energy range 7.55–7.6 eV.
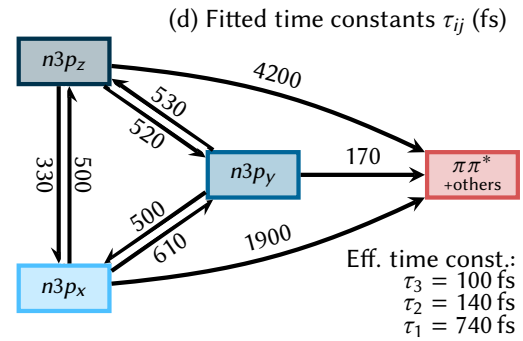


Figure S17: Results of the global fit of the electronic populations in the energy range 7.6–7.7 eV.

Figure S18: Results of the global fit of the electronic populations in the energy range 7.7–7.8 eV.
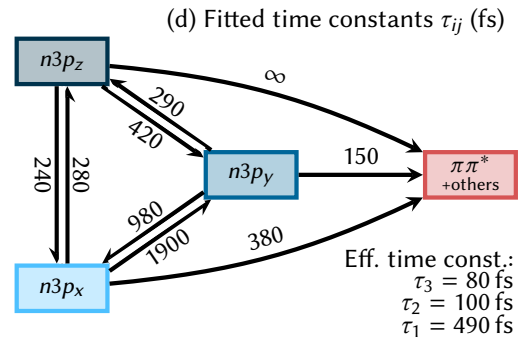


Figure S19: Results of the global fit of the electronic populations in the energy range 7.8–8.0 eV.
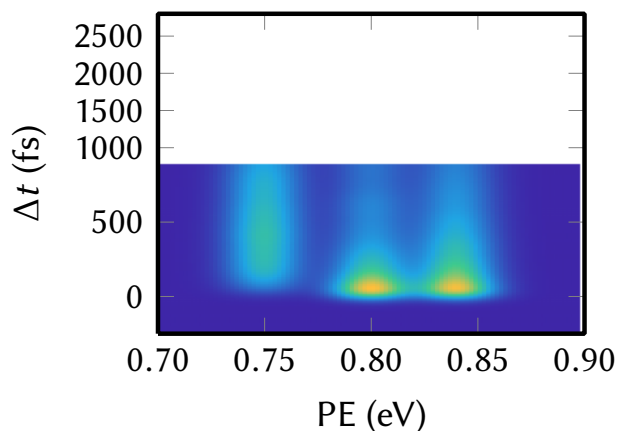
Figure S20: Time-resolved photoelectron spectrum simulated from the diabatic populations obtained with the SHARC computations (0.52 times the ensemble starting in n3p$_y$ plus 0.48 times the ensemble starting in n3p$_z$). The spectrum assumes identical photoionization probabilities for all three Rydberg states.

# References

(S1) van Stokkum, I. H.; Larsen, D. S.; van Grondelle, R. *Biochem. Biophys. Acta Bioenergetics* **2004**, *1657*, 82 – 104.

(S2) Wu, G.; Boguslavskiy, A. E.; Schalk, O.; Schuurman, M. S.; Stolow, A. *J. Chem. Phys.* **2011**, *135*, 164309.

(S3) Nobre, M.; Fernandes, A.; da Silva, F. F.; Antunes, R.; Almeida, D.; Kokhan, V.; Hoffmann, S. V.; Mason, N.; Eden, S.; Limão-Vieira, P. *Phys. Chem. Chem. Phys.* **2008**, *10*, 550–560.

(S4) Köppel, H.; Domcke, W.; Cederbaum, L. S. *Adv. Chem. Phys.*; John Wiley & Sons, Inc., 1984; Vol. 57; pp 59–246.

(S5) Plasser, F.; Goméz, S.; Mai, S.; González, L. *Phys. Chem. Chem. Phys.* **2019**, *21*, 57–69.

(S6) Dreuw, A.; Wormit, M. *WIREs Comput. Mol. Sci.* **2015**, *5*, 82–95.

(S7) Dunning, T. H. *J. Chem. Phys.* **1989**, *90*, 1007–1023.

(S8) Kaufmann, K.; Baumeister, W.; Jungen, M. *J. Phys. B: At. Mol. Phys.* **1989**, *22*, 2223.

(S9) TURBOMOLE V7.0, A development of University of Karlsruhe and Forschungszentrum Karlsruhe GmbH. 2015.

(S10) Fumanal, M.; Plasser, F.; Mai, S.; Daniel, C.; Gindensperger, E. *J. Chem. Phys.* **2018**, *148*, 124119.

(S11) Plasser, F.; Ruckenbauer, M.; Mai, S.; Oppel, M.; Marquetand, P.; González, L. *J. Chem. Theory Comput.* **2016**, *12*, 1207.

(S12) Barbatti, M.; Granucci, G.; Persico, M.; Ruckenbauer, M.; Vazdar, M.; Eckert-Maksić, M.; Lischka, H. *J. Photochem. Photobiol. A* **2007**, *190*, 228–240.

(S13) Granucci, G.; Persico, M.; Toniolo, A. *J. Chem. Phys.* **2001**, *114*, 10608–10615.

(S14) Granucci, G.; Persico, M. *J. Chem. Phys.* **2007**, *126*, 134114.

(S15) Dormand, J.; Prince, P. *J. Comput. Appl. Math.* **1980**, *6*, 19 – 26.

(S16) Branch, M.; Coleman, T.; Li, Y. *SIAM J. Sci. Comput.* **1999**, *21*, 1–23.

(S17) Nangia, S.; Jasper, A. W.; Miller, T. F.; Truhlar, D. G. *J. Chem. Phys.* **2004**, *120*, 3586–3597.

(S18) Mai, S.; Marquetand, P.; González, L. *J. Phys. Chem. Lett.* **2016**, *7*, 1978–1983.